Prediction of the Fuel Regression-Rate in a HDPE Single Port Hybrid Rocket Fed by Liquid Nitrous Oxide

Giuseppe Gallo[1], Landon Kamps[2], Shota Hirai[3], Carmine Carmicino[4], Nagata Harunori[5]
Hokkaido University, Sapporo, Hokkaido, 060-8628, Japan.

Abstract

This paper presents a computational thermo-fluid-dynamic model of the hybrid rocket internal ballistics, which was developed with the specific aim of predicting the axial position and severity of the increased fuel-consumption spots observed in static engine firings. Numerical simulations of the internal flow field have been carried out on the configuration of the engine previously fired. The novelty of this work consists in providing a simplified methodology to calculate the regression rate measured burning liquid nitrous oxide with high-density polyethylene, which involves a series of additional complexities with respect to the case of pure gaseous oxygen (i.e., a non-decomposing oxidizer). Indeed, the typical non-premixed flame developed in the chamber is preceded by a decomposition reaction of the nitrous oxide, whose simulation implies further numerical cost. For the validation of the model, data retrieved from two firing tests are compared with the numerical results revealing good agreement of both the average regression rate and fuel consumption axial profile. A dedicated study was performed to assess the reliability of the assumptions underlying the model. Results are also compared with those obtained with either pure oxygen or 85wt% hydrogen peroxide. Finally, a different prechamber arrangement was suggested to address the issue deriving from excessive fuel regression.

---

[1] JSPS International Fellow, Department of Mechanical and Space Engineering, and AIAA Member.

[2] Specially Appointed Assistant Professor, Department of Mechanical and Space Engineering, and AIAA Member.

[3] PhD Student, Department of Mechanical and Space Engineering, and AIAA Member.

[4] Freelance Research Consultant.

[5] Professor, Department of Mechanical and Space Engineering, and AIAA Member.

Nomenclature

A	= regression rate pre-exponential factor, mm/s
A_t	= throat area, m^2
c	= specific heat, J/kg·K
c^*	= characteristic velocity, m/s
D	= fuel grain port diameter, mm
D_1	= fuel grain port initial diameter, mm
D_2	= fuel grain port average final diameter, mm
E_a	= activation energy, J/mol
f	= average mixture fraction
f'^2	= mixture fraction variance
G	= mass flux, $kg/m^2 \cdot s$
h	= heat transfer coefficient, $W/m^2 \cdot K$
L	= fuel grain length, mm
$\dot{m}$	= mass flow rate, g/s
M	= total vessel mass, kg
n	= normal-to-surface coordinate oriented from solid to gas, m
OF	= mixture ratio
p	= pressure, Pa
Pr_t	= turbulent Prandtl number
$\dot{q}$	= heat flux, W/m^2
R	= universal gas constant, J/K·mol
$\mathcal{R}$	= Reynolds stress tensor, $kg/(m \cdot s^2)$
Re	= Reynolds number
Re_t	= turbulent Reynolds number
$\dot{r}$	= fuel regression rate, mm/s
Sc_t	= turbulent Schmidt number
T	= temperature, K
t	= time, s
v	= gas velocity component normal to surface, m/s
x, y	= generic coordinate, m

Greek Symbols

β	= Temperature exponent
Δ	= grid node displacement, mm
h_p	= fuel heat of pyrolysis, J/kg
Δt	= time-step, s
λ	= thermal conductivity
μ_t	= turbulent viscosity, kg/m·s
ϑ	= local grain surface inclination, rad
ρ	= gas density, kg/m^3

Superscripts

$\bar{}$	= time average
$\tilde{}$	= density-weighted average

Subscripts

b	= burning time
c	= chamber
f	= fuel
w	= wall

1. Introduction

Hybrid rocket engines (HRE) are chemical propulsion systems employing two propellants in separate phases. In the classical system arrangement, the fuel is stored in the combustion chamber in the solid phase and a gaseous or liquid oxidizer is injected into the port of the solid fuel grain. An in-depth trade off analysis was performed by Kamps et al.[1] for the choice of the most suitable oxidizer maximizing the velocity increment within a fixed envelope size. The results showed that nitrous oxide (N_2O) and hydrogen peroxide (H_2O_2) outperform other oxidizers like oxygen and di-nitrogen tetroxide (N_2O_4). However, N_2O has an additional unique feature: the high vapor pressure at room temperature (i.e., 55.5 atm at 25°C) allows for self-pressurization, usually making N_2O an ideal propellant for small propulsion systems for which the simplicity is an advantage over the lower specific impulse performance compared to higher-energy oxidizers such as oxygen. For this reason, the authors focused their efforts on maximizing performance of HREs working with N_2O. The authors are currently involved in the design

and testing of hybrid rocket kick-motors operating for relatively long durations, upwards of 70 s at a time, using liquid nitrous oxide as oxidizer and high-density polyethylene as fuel. An extensive experimental campaign was carried out reporting histories for fuel mass consumption, nozzle throat erosion, characteristic exhaust velocity efficiency, and nozzle throat wall temperature [2]. Additional studies provided fuel regression rate correlations and combustion characteristics in conventional and non-conventional HRE configurations [3,4].

Many noteworthy hybrid rocket demonstrations in recent years have been achieved in part by taking advantage of the self-pressurizing ability of N_2O. These include the SpaceShipTwo, as well as its predecessor vehicle, SpaceShipOne [5], the highly successful Stuttgart University student-based hybrid sounding rocket, HEROS 3, reported by Kobald et al. [6], the rocket test sled trials of Muroran Institute of Technology reported by Nakata et al. [7], the small launch vehicles of TiSPACE Inc. reported by Chen and Wu [8], as well as the sounding rockets of Space Forest Ltd. reported by Gamal et al. [9].

Regarding the selection of the fuel material and the design of the fuel grain shape, the regression rate is one of the key decision-making parameters, since it constrains the fuel mass consumption rate in response to the oxidizer supply rate, the combination of which determines the thrust and ideal specific impulse. At the initial design stage, spatially-averaged fuel regression rate correlations are used to simplify estimates for overall system size and mass specifications. Moreover, in many cases, the only correlations available in the open literature are expressed in terms of time- and space-averaged parameters, due to constraints in the experimental methodology of the works. Nonetheless, in practice, local regression rate prediction becomes crucial for realistic performance estimations, and for guaranteeing engine safety and reliability.

Significant non-uniformity of fuel regression was exhibited in the first long burning-time experiments – i.e., greater than 25 s, for which multiple previous experimental works have been published – conducted by the authors. Some specific sections of the grain had significantly higher regression rates, which must be taken into account to ensure appropriate thermal insulation of the thrust chamber casing and, thus, safe engine operation. In other words, unexpected enhancements of the regression rate can jeopardize the reliability of the overall propulsion system, because the fuel grain is a thermal shield for the metallic case. Hence, mastering the prediction and/or reproduction of the internal ballistics allows improving the engine design in terms of both performance and system safety.

From a physical point of view, with pyrolyzing fuels (i.e., the class of materials whose inner surface does not liquefy under the engine operating conditions), the regression rate is the rate at which the fuel is gasified. The flow field that is established in the combustion chamber determines the heat flux to the grain surface exposed to the hot gases, which is an input for the regression rate model. In particular, the injector-prechamber configuration qualitatively and quantitatively influences the wall heat flux, especially in the low aspect-ratio motors. Internal ballistics calculations based on the classical boundary-layer theory [10], even when applied to simple engine arrangements, in which a head-end injector is set up and an axial mean flow is established in the fuel port, can fail to predict the actual engine performance for the lack of the oxidizer-injection fluid dynamics modelling [11,12, 13].

Although simplified regression rate correlations are usually employed during the design phase, they do not allow for accurate evaluation of the local trend of fuel consumption, hence more sophisticated numerical methods are required, such as computational-fluid-dynamic (CFD) simulations. CFD modelling of the flow field in the combustion chamber of a hybrid propellant rocket has been the subject of considerable interest in recent years [14,15,16,17,18], but, due to the demanding computational costs and complexity, comprehensive models to describe the detailed interactions among fluid dynamics [19], fuel grain pyrolysis [20], liquid oxidizer atomization and vaporization, mixing and combustion in the gas phase [21], nozzle

thermochemical erosion [22], particulate formation, and radiative characteristics of the flame [17,23] are still a subject of research and deliberation.

However, it is clear from previous research that CFD analyses can be tailored to predict the regression rate with reasonable accuracy by introducing appropriate simplifications, which allows researchers to correctly estimate the incident wall heat flux on the fuel grain surface resulting from the combustion and the blowing phenomena in the boundary layer. The main structure of the numerical setup presented in this work (i.e., turbulence and combustion modelling) was validated in past works on different engine operating conditions and different types of fuels (classic pyrolyzing polymers and liquefying ones, with two different fuel surface treatments to also consider the effect of the liquid-fuel entrainment which occurs in the latter case) [24,25,26,27]. The novelty of the current work is in the modelling of the nitrous oxide combustion with high-density polyethylene (HDPE) and the introduction of some simplifications to overcome the additional burden introduced by the injection of the oxidizer in the liquid phase.

The results have been validated on two experimental test cases. The tests have been carried out in the same operating conditions with largely different burning times. The assessment on this particular test series highlights the validity of our numerical model for long burning durations. Numerical predictions of regression rate profiles are compared with experimental measurements for a full validation.

The work is presented with the following structure:

- Firstly, the experimental set-up and tests are described.
- Secondly, the numerical apparatus, which consists of a CFD code coupled with a suitable gas surface interface (GSI) model, is defined. In addition, all the simplifications introduced to solve the limitations of the numerical model are described.
- Finally, the numerical results are compared with the experimental data. The effect of the injection system and of the prechamber on the regression rate distribution is discussed and some modifications are indicated to mitigate the observed issues.

2. Experimental Firing Tests

The test facility is a versatile setup designed primarily for testing hybrid rocket engines of several sizes. It is equipped with a test rig and a general-purpose acquisition system, which allows evaluating engine performance. A schematic of the hybrid rocket employed in this work is depicted in Figure 1.

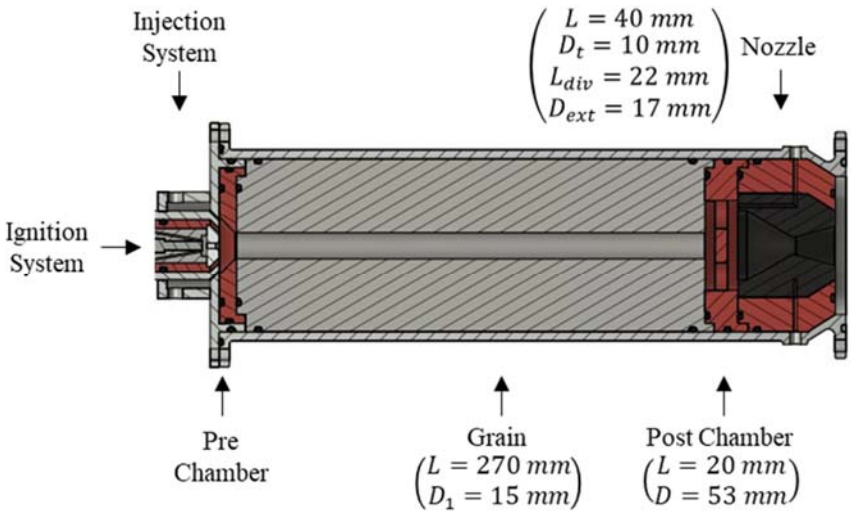

Figure 1 Hybrid rocket layout.

The rocket engine has an axisymmetric combustion chamber, around 350-mm in length and 100-mm in (inner) diameter. The liquid nitrous oxide is supplied to the chamber from the tanks in a self-pressurized fashion. The injector manifold has 8 holes arrayed uniformly around the engine axis at an angle of 45 deg and a diameter of 0.8 mm, through which nitrous oxide is delivered to a single-port cylindrical fuel grain of HDPE. A converging pre-combustion chamber and an aft-mixing chamber are set up upstream and downstream of the solid grain, respectively, which are made by thermal insulation materials in order to withstand the high temperature of the combustion gas. The post-chamber is a multi-perforated short disk which promotes unburned propellant mixing. A graphite converging-diverging exhaust nozzle is employed, whose throat and exit section diameters are 10 mm and 17 mm, respectively.

Chamber pressure is measured by means of two Kyowa PHB-A-10MP pressure transducers, one which is installed in the pre-chamber, and one which is installed at the exit of an access port running through the nozzle. An igniter is placed on the axis. Details of the ignitor concept can be found in Ref. [28]. It consists of a miniaturized version of the current hybrid rocket equipped with a glow plug and placed on the motor axis (see Figure 1). So, firstly the ignition is triggered in the small-scale motor by using the glow plug; then, the exhausted combustion gases are directly injected into the main combustion chamber starting the firing test. The combustion gases created in the igniter, which operates for around 8 s, are used to gasify the main fuel grain for combustion with the main oxidizer flow. The oxidizer mass flow rate was evaluated by computing the time derivative of the measured oxidizer tanks' mass during the burning time, after best fitting the raw data.

2.1. Firing Test Cases

Two different firing tests performed at the same operating conditions with different burning times are considered as test cases for the validation of the numerical model, both of which use HDPE and liquid nitrous oxide as propellants. The fuel grain length was equal to L = 270 mm and the initial port diameter was equal to D_1 = 15 mm. The test durations were set to 45 s (Test 1) and 70 s (Test 2). A picture of the rocket exhaust plume for the 45 s firing test is shown in Figure 2.

Figure 2. Rocket exhaust plume (Test 1).

Figure 3a displays a comparison of the pressure traces between the two tests. The ignition system operated in the first 8 seconds for both the tests. Hot gases exhausted by the ignition system when injected into the chamber involve an anomalous enhancement of the regression rate during the ignition phase, which is discussed in the next sections. The chamber pressure signals regularly decrease in both the tests. No nozzle erosion was observed in either test. Figure 3b displays the tank mass during the burning time. As shown, while a stable trace was observed until 45 s for both the tests, oscillations are shown in the last seconds for the longer test, which indicate the emptying of the tanks. On average, over this oscillation period, the oxidizer mass flow rate is slightly lower, accordingly, the pressure trace of Test 2 decreases more rapidly in the last 10 seconds or so. The resulting mass flow rate, evaluated as explained above, is 0.0538 kg/s and 0.0509 kg/s in Test 1 and Test 2, respectively.

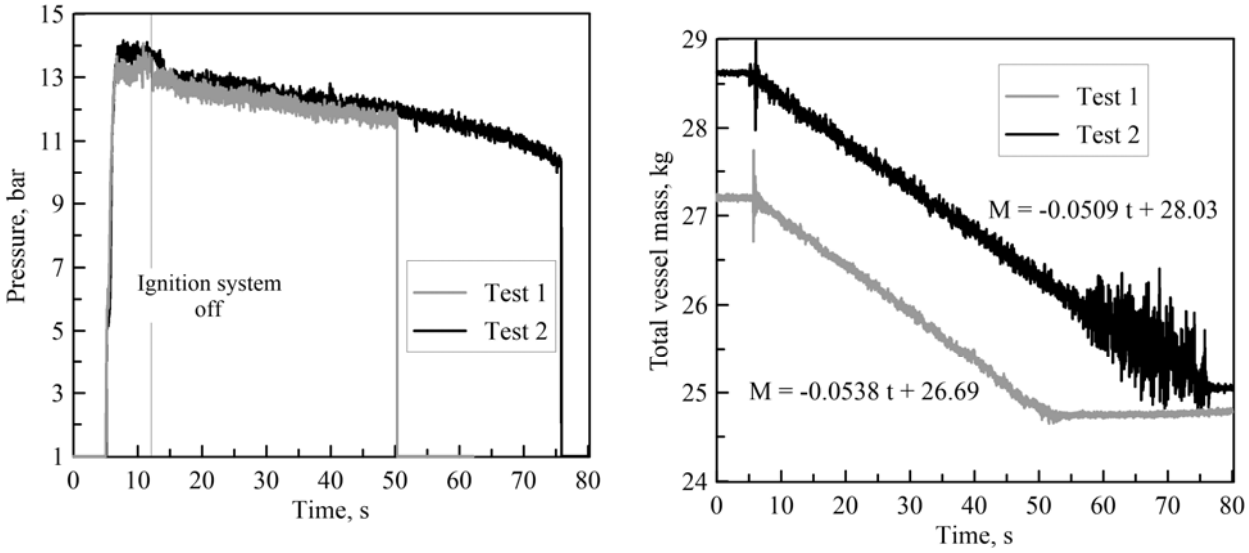

(a) Operating pressure. **(b) Oxidizer tank weight.**

Figure 3. Experimental signals during the burning time.

Figure 4 displays the comparison of the regression rate spatial profiles of the two tests. The experimental profiles have been obtained by sectioning the grain length in 6 slices – i.e., at intervals of approximately 45 mm. The represented points are given at the interface of each slice by averaging the measured outlet diameter of the upstream slice with the inlet of the next one. The outlet and inlet diameters of the grain slices are obtained by averaging four measurements of the local diameter as

well. Therefore, the average final local diameter, $\overline{D}_2$, is the result of the averaging of eight measurements. Then, the regression rate is computed as:

$$\dot{r} = \frac{\overline{D}_2 - D_1}{2t_b} \tag{1}$$

where D_1 is the initial diameter and t_b is the burning time. The largest and smallest values of the error bars displayed in Figure 4 are evaluated by using the largest and smallest diameter of the eight local measurements. Therefore, a large error band indicates the deviation of the local consumption from a perfect axisymmetric regression.

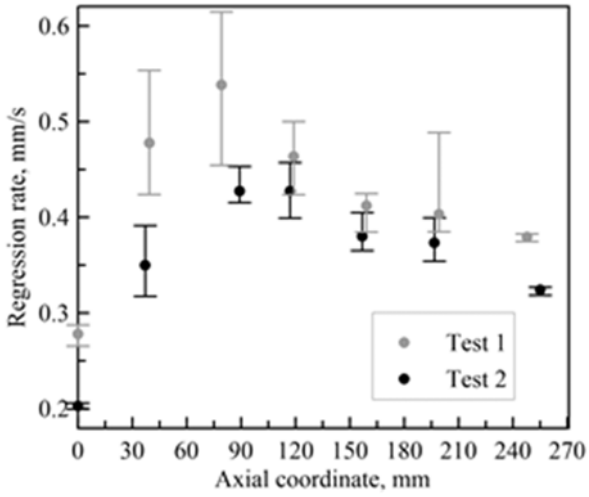

Figure 4 Regression rate spatial profiles of Test 1 and Test 2.

It can be noticed that both the regression rate profiles are highly non-uniform along the grain length, and they feature a peak in the first half of the grain, i.e., around 80 mm in Test 1 and 90 mm in Test 2. The qualitative and quantitative prediction of the peak is extremely important for the design of the fuel grain thickness. Figure 5 displays the fuel grain shape at the end of the burning. Figure 5b clearly justifies the motivation of the current work. A slightly longer burning time would have led to the exposure of the engine casing to combustion gas, and subsequent structural failure due to overheating.

(a) **(b)** **(c)**

Figure 5 Pictures of the fuel grain at the end of the burning in Test 2.

Finally, the average parameters measured in the two tests are summarized in Table 1. The time- and spatially-averaged regression rates were obtained both by means of the mass loss method [11] and a caliper through averaging the points displayed in Figure 4. Note that, because a considerable amount of fuel mass has been lost during the extraction of the fuel grain, in particular in the zone close to the post-chamber and nozzle, both the estimations are presented in this work. The burning time was defined as the time duration between the chamber pressure rise and fall at the beginning and end of the test, respectively.

Table 1. Firing test operating conditions.

Parameter	Test 1	Test 2
Time-averaged oxygen mass flow rate, g/s	53.8	50.9
Burning time, s	45.3 ± 2.61	70.71 ± 2.68
Average Mixture Ratio	3.97 ± 0.23	4.08 ± 0.15
Time-space averaged regression rate, mm/s	0.422* ± 0.021 0.467** ± 0.11	0.355* ± 0.014 0.401** ± 0.08
Time-averaged pre-chamber pressure, bar	12.34 ± 0.07	12.45 ± 0.07
Characteristic exhaust velocity, m/s	1422 ± 16	1441 ± 10

* Based on the caliper measurement averaging.

** Based on the fuel mass loss measurement.

3. Fuel Regression-Rate Calculation Methodology

The key parameter dealt with in this paper is the fuel grain regression rate. As mentioned above, for a given pyrolyzing fuel, regression rate is basically limited by the heat flux input to the solid grain, which mostly depends on the thermo-fluid dynamics in the combustion chamber and on the regression rate itself, through the convective heat transfer blocking. Hence, the overall numerical approach consists mainly in the integration of two tools, which are a CFD model for the evaluation of the incident wall heat flux on the grain surface, and a GSI treatment for the computation of the regression rate. The main feature of the CFD model is the strong coupling of the turbulence with the combustion model, which allows us to take into account the enhancing effects of recirculation zones due to the inlet flow pattern into the grain port [29]. A transient, quasi-steady state procedure is applied, which allows calculating the regression rate during the burning time.

3.1. CFD Numerical Apparatus

The main purpose of the CFD analysis presented in this work, as mentioned above, is the computation of the thermo-fluid dynamic field developed into the combustion chamber. In this work, the computational domain includes the entire internal engine volume with the exception of the pre-chamber, in which it is assumed that no combustion occurs. Note that, in the specific engine configuration considered here, the pre-chamber extension is very short compared to the overall combustion

chamber length and it is installed to feed the oxidizer properly into the fuel grain port (see Figure 1, and Figure 6 that follows in the discussion of the injection arrangement in Sec. 3.3); its effect on the engine internal ballistics is assumed negligible and, thus, it is basically considered a part of the engine through which the oxidizer completely flashes into the gaseous phase before burning into the combustion chamber. The pyrolysis process of the plastic fuel grain is treated by means of a suitable GSI model described in the next subsection. Although the actual products of solid fuel phase change are numerous and their composition depends on the heating rate, here, gaseous ethylene has been used to represent the fuel injected from the grain surface, since it does not differ significantly in terms of reaction balancing with respect to a generic normal-alkane C_nH_{2n+2} material with a high carbon number. The Reynolds-Averaged Navier–Stokes (RANS) equations for single-phase multicomponent turbulent reacting flows are solved with a control-volume-based technique and a pressure-based algorithm [30]. The Favre-averaged equations of continuity and momentum with a mass flow rate source term can be written in Cartesian tensor form as [31, 32]:

$$\frac{\partial \bar{\rho}}{\partial t} + \frac{\partial}{\partial x_j}\left(\bar{\rho}\tilde{u}_j\right) = S_m \tag{2}$$

$$\frac{\partial}{\partial t}\left(\bar{\rho}\tilde{u}_i\right) + \frac{\partial}{\partial x_j}\left(\bar{\rho}\tilde{u}_i\tilde{u}_j\right) = -\frac{\partial \bar{p}}{\partial x_i} + \frac{\partial \bar{\tau}_{ij}}{\partial x_j} + \frac{\partial}{\partial x_j}\left(-\overline{\rho u_i' u_j'}\right) + S_m\tilde{u}_i \tag{3}$$

where S_m is the source term, i.e., the fuel mass flow rate added to the gas phase, and the repeated indices mean summation. Furthermore, the overbar indicates time averaging, while the tilde indicates density-weighted averaging. The stress tensor, τ_{ij}, is expressed as

$$\tau_{ij} = \mu\left[\left(\frac{\partial u_i}{\partial x_j} + \frac{\partial u_j}{\partial x_i}\right) - \frac{2}{3}\delta_{ij}\frac{\partial u_k}{\partial x_k}\right] \tag{4}$$

Where δ_{ij} is the Kronecker delta. The Reynolds stress tensor, $\mathcal{R}_{ij} = -\overline{\rho u_i' u_j'}$, requires to be modeled.

The Shear Stress Transport (SST) turbulence model [33] has been employed for its improved capability of predicting flows with separated regions. It a combination of the robust and accurate *k–ω* model, developed by Wilcox [34], in the near-wall region, with the standard *k–ε* model implemented away from the wall using a blending function. The transport equations of the turbulence kinetic energy, k, and the specific dissipation rate, ω, are formulated as

$$\frac{\partial}{\partial t}(\bar{\rho}k) + \frac{\partial}{\partial x_i}(\bar{\rho}\tilde{u}_i k) = \frac{\partial}{\partial x_j}\left[(\mu + \mu_t\sigma_k)\frac{\partial k}{\partial x_j}\right] + \mathcal{R}_{ij}\frac{\partial \tilde{u}_i}{\partial x_j} - \beta^*\bar{\rho}\omega k \tag{5}$$

$$\frac{\partial}{\partial t}(\bar{\rho}\omega) + \frac{\partial}{\partial x_i}(\bar{\rho}\tilde{u}_i\omega) = \frac{\partial}{\partial x_j}\left[(\mu + \mu_t\sigma_\omega)\frac{\partial \omega}{\partial x_j}\right] + \bar{\rho}\frac{\alpha}{\mu_t}\mathcal{R}_{ij}\frac{\partial \tilde{u}_i}{\partial x_j} - \beta\bar{\rho}\omega^2 + 2(1-F_1)\bar{\rho}\sigma_{\omega_2}\frac{1}{\omega}\frac{\partial k}{\partial x_j}\frac{\partial \omega}{\partial x_j} \tag{6}$$

Where the tensor, $\mathcal{R}_{ij}$, is defined using the Boussinesq approximation

$$\mathcal{R}_{ij} = \mu_t\left[\left(\frac{\partial \tilde{u}_i}{\partial x_j} + \frac{\partial \tilde{u}_j}{\partial x_i}\right) - \frac{2}{3}\delta_{ij}\frac{\partial \tilde{u}_l}{\partial x_l}\right] - \frac{2}{3}\bar{\rho}k\delta_{ij} \tag{7}$$

The turbulent viscosity, μ_t, is expressed as follows

$$\mu_t = \frac{\bar{\rho}k}{\omega}\frac{1}{max\left(1; \frac{\Omega F_2}{0.31\omega}\right)} \tag{8}$$

where the function F_2 is defined, depending on the distance from the wall y, as

$$F_2 = tanh(\Phi_2^2) \tag{9}$$

with

$$\Phi_2 = max\left(\frac{2\sqrt{k}}{0.09\omega y}; \frac{500\mu}{\bar{\rho}\omega y^2}\right) \tag{10}$$

The coefficient α is given by

$$\alpha = \gamma \frac{1/9 + Re_t/2.95}{1 + Re_t/2.95} \tag{11}$$

where $Re_t = \bar{\rho}k/\mu\omega$ is the turbulent Reynolds number. The blending function F_1 takes the value of 1 on the wall and tends to zero at the boundary layer edge, being defined as

$$F_1 = tanh(\Phi_1^4) \tag{12}$$

with

$$\Phi_1 = min\left[max\left(\frac{\sqrt{k}}{0.09\omega y}; \frac{500\mu}{\bar{\rho}\omega y^2}\right); \frac{4\bar{\rho}\sigma_{\omega_2}k}{CD_{k\omega}y^2}\right] \tag{13}$$

where $CD_{k\omega}$ is the positive part of the last term in Eq. (6) (cross-diffusion term):

$$CD_{k\omega} = max\left(2\bar{\rho}\sigma_{\omega_2}\frac{1}{\omega}\frac{\partial k}{\partial x_j}\frac{\partial \omega}{\partial x_j}; 10^{-20}\right) \tag{14}$$

The model coefficients σ_k, σ_ω, β, γ are defined by blending the corresponding coefficients of the original *k–ω* model, denoted with the subscript 1, with those of the transformed *k–ε* model that are denoted with the subscript 2:

$$\begin{bmatrix}\sigma_k \\ \sigma_\omega \\ \beta \\ \gamma\end{bmatrix} = F_1\begin{bmatrix}\sigma_{k_1} \\ \sigma_{\omega_1} \\ \beta_1 \\ \gamma_1\end{bmatrix} + (1 - F_1)\begin{bmatrix}\sigma_{k_2} \\ \sigma_{\omega_2} \\ \beta_2 \\ \gamma_2\end{bmatrix} \tag{15}$$

All the model constants are listed in Table 2.

Table 2 Values of SST model constants [31].

Constant	Value	Constant	Value
σ_{k_1}	0.850	σ_{k_2}	1.00
σ_{ω_1}	0.500	σ_{ω_2}	0.856
β_1	0.075	β_2	0.0828
γ_1	0.553	γ_2	0.440
β^*	0.090		

Because it is assumed that the chemical kinetics are fast compared to the diffusion processes occurring in the combustion chamber for the typical mass fluxes and pressures considered here [35], the non-premixed combustion of nitrous oxide and the gaseous fuel injected from the grain wall is modelled by means of the Probability Density Function (PDF) approach coupled to chemical equilibrium [36]. Accordingly, combustion is simplified to a mixing problem (mixed is burnt), and the difficulties associated with closing non-linear reaction rates are avoided. Assuming the Lewis number is unity, and equal diffusivities for all the species, the species conservation equation can be reduced to a single equation by the definition of the mixture fraction as, $f = 1/(1 + OF)$, where *OF* is the local oxidizer-to-fuel mass ratio for the equivalent non-burning field. The mean mixture fraction equation can be expressed as

$$\frac{\partial}{\partial t}\left(\bar{\rho}\tilde{f}\right)+\frac{\partial}{\partial x_j}\left(\bar{\rho}\tilde{u}_j\tilde{f}\right)=\frac{\partial}{\partial x_j}\left(\frac{\mu_t}{Pr_t}\frac{\partial\tilde{f}}{\partial x_j}\right)+S_m \tag{16}$$

The turbulence-chemistry interactions are described by means of the mixture fraction variance, f''^2 , which is described by an additional equation, which, according to [37], can be expressed as

$$\frac{\partial}{\partial t}\left(\bar{\rho}\widetilde{f''^2}\right)+\frac{\partial}{\partial x_j}\left(\bar{\rho}\tilde{u}_j\widetilde{f''^2}\right)=\frac{\partial}{\partial x_j}\left(\frac{\mu_t}{Pr_t}\frac{\partial\widetilde{f''^2}}{\partial x_j}\right)+2\frac{\mu_t}{Pr_t}\left(\frac{\partial\tilde{f}}{\partial x_j}\right)^2-2\beta^*\bar{\rho}\omega\widetilde{f''^2} \tag{17}$$

The shape of the assumed PDF is described by the β-function of the mean mixture fraction and its variance [38]. Finally, a governing equation for the total enthalpy is required because the system can lose energy at the grain boundary, which affects the computation of the temperature and the species fractions.

Finally, the energy equation can be expressed as:

$$\frac{\partial}{\partial t}\left(\bar{\rho}\tilde{E}\right)+\frac{\partial}{\partial x_j}\left(\bar{\rho}\tilde{u}_j\tilde{H}\right)=\frac{\partial\tilde{u}_i\left(\tilde{\tau}_{ij}\right)_{eff}}{\partial x_j}-\frac{\partial\tilde{q}}{\partial x_j}+S_m\tilde{H}+S_h \tag{18}$$

$$\tilde{q}=-k_{eff}\frac{\partial\tilde{T}}{\partial x_j}+\sum_k\left(\left(h_k^0(T_{ref,k})+\widetilde{h_k}\right)\left(\frac{\mu}{Sc}\right)_{eff}\frac{\partial\tilde{Y}_k}{\partial x_j}\right) \tag{19}$$

where the turbulent Prandtl number, Pr_t, is set to 0.85, the laminar and turbulent Schmidt number are set to 0.7, Y_k is the species mass fraction, h_k^0 is the species formation enthalpy and S_h is enthalpy associated to the heat of phase change. The subscript, *eff,* indicates that all the physical properties included in the corresponding quantities are the sum of the laminar and turbulent component (e.g. $k_{eff} = k + k_t$).

The instantaneous total enthalpy, H, and total energy, E, are given by:

$$H=\sum_k Y_k\left(h_k^0(T_{ref,k})+h_k\right)+\frac{{u_i}^2}{2}=\sum_k Y_k\left(h_k^0(T_{ref,k})+\int_{T_{ref,k}}^{T}c_{p,k}(T)dT\right)+\frac{{u_i}^2}{2} \tag{20}$$

$$E=H-\frac{p}{\rho} \tag{21}$$

The temperature dependence of the specific isobaric heat capacities of the species is expressed by a fourth degree polynomial:

$$c_p(T)=A_1+A_2T+A_3T^2+A_4T^3+A_5T^4 \tag{22}$$

Two sets of coefficients, A, are included in the solver for each species, of which the first is valid in a range between 300 and 1000 K, while the second in a range between 1000 and 5000 K.

Once f, f''^2 and H are calculated at each point in the flow field, the known PDF is used to compute the time-averaged values of individual species mole fractions and temperature with simple thermochemistry calculations based on the minimization of Gibbs free energy [39]. Then, the density is obtained by the means of the thermal equation of state:

$$\rho=\frac{\mathrm{p}}{\left(R/\left(\sum_k\frac{Y_k}{M_k}\right)^{-1}\right)T} \tag{23}$$

Molecular weights, and enthalpies of formation for each species considered are extracted from the solver chemical database; the mixture specific heat is determined via the mixing law. Molecular dynamic viscosities and thermal conductivities of each species are calculated as functions of local temperature, according to Ref. [39].

3.2.GSI Model

Once the wall heat flux on the fuel grain surface is computed, the regression rate and wall temperature are evaluated by an ad-hoc interface model. The GSI model is the conjunction ring between the gaseous flow region and the solid fuel wall, since it describes the pyrolysis phenomenon. It is known that the pyrolysis products are numerous and their composition depends on the pyrolysis temperature [14,15], however, gaseous ethylene (C_2H_4) is known to be the predominant species. For this reason, only gaseous ethylene is involved in the numerical analysis. The fuel surface can be schematized as an inlet boundary along which the fuel mass flux, the temperature, and the mixture fraction are unknown. The mass conservation at the gas-solid interface over a pyrolyzing fuel grain imposes that

$$(\rho v)_w = \rho_f \dot{r} \tag{24}$$

where ρ is the gas density at the wall, and v is the normal-to-wall velocity component due to the pyrolysis products injection; ρ_f is the solid fuel density and $\dot{r}$ is the local regression rate.

The GSI model consists of two equations: an energy balance equation at the gas-solid interface and an Arrhenius-like formula for the regression rate. Regarding the former, it takes into account the convective heat transfer from the gas to the fuel surface and the heat conduction into the solid grain. The radiation contribution is neglected, because, under the large oxygen mass fluxes realized in the considered firing tests, it is expected to produce second order effects with the non-metallized propellant burned here – radiation flux on the order of 20% of the convective mass flux provides a regression rate enhancement of 5% [40,41]. Assuming the axial component of the heat conduction, the normal area variation in the grain cylinder, and the dependency of the fuel thermal properties on the temperature all to be negligible, the energy balance equation is given by [26]

$$\dot{q}_w = \left(k_g \frac{\partial T}{\partial n}\right)_w = \rho_f \dot{r}\left[\Delta h_p + c_f(T_w - T_{wi})\right] \tag{25}$$

where Δh_p is the so-called heat of pyrolysis, T_w is the fuel surface temperature, and T_{wi} is its initial temperature (which is assumed equal to that of the external surface of the fuel). Usually, the term in brackets at the right-hand side is indicated by $h_v = \Delta h_p + c_f(T_w - T_{wi})$, and it represents the effective heat of gasification of the fuel, which, in addition to the heat of pyrolysis, accounts for the heat conducted into the solid grain.

Finally, the fuel pyrolysis is modeled with the following semi-empirical Arrhenius-type equation [27]

$$\dot{r} = A \cdot \exp\left(-\frac{E_a}{2RT_w}\right) \tag{26}$$

where A is the pre-exponential factor, E_a is the activation energy and R is the universal gas constant.

The values of the constants appearing in Eq. (25) and Eq. (26) considered for the HDPE fuel grain analyzed in this work are summarized in Table 3. Density, specific heat and heat of pyrolysis are taken from the work in Ref. [42], while the values of the pre-exponential factor and the activation energy from Ref. [20] by modifying the activation energy to match the surface

temperature commonly observed in polymeric hybrid fuels (which is around 800 K) [43]. In fact, pyrolysis data are highly sensitive to the heating rate and they are usually obtained with heating rates several orders of magnitude lower than those involved in hybrid rockets, thus some differences may be expected. However, calculations performed with the original value of the activation energy, despite providing similar regression rates, yielded corresponding fuel surface temperatures significantly higher.

Table 3 HDPE material properties and rate constants.

Density, ρ_f kg/m^3	Specific heat, c_f J/kg K	Heat of pyrolysis, Δh_p MJ/kg	Initial fuel temperature, T_{wi} K	Pre-exponential factor, A mm/s	Activation Energy, E_a, kJ/mol
950	2833	4.045	300	$4.78 \cdot 10^6$	190

As outlined previously, from Eq. (26), for the very large value of the ratio E_a/R (Table 3), significant regression rate changes can be produced with minor changes in the surface temperature. Once Eq. (25) and Eq. (26) are combined, given the heat flux to the wall from the flow field solution, both the fuel surface temperature and the regression rate can be determined.

An additional equation for the mean mixture-fraction balance at the gas-solid interface is needed, which states the fact that the total mass flux entering the gaseous domain due to the solid fuel consumption is partially balanced by the convection and partially by the diffusion of the fuel mass fraction, as expressed by Eq. (27):

$$(\rho v)_w f_w - \left(\frac{\mu_t}{Sc_t}\frac{\partial f}{\partial n}\right)_w = \rho_f \dot{r} \tag{27}$$

The balance of the mixture-fraction variance, $\widetilde{f''^2}$, at the wall is instead ignored and the latter is imposed to be zero. As the flow field depends on all the parameters at the fuel wall, an iterative procedure is needed to determine the solution.

3.3. Assumptions and Simplifications

As already mentioned, the nitrous oxide is self-pressurized into the engine in the tests considered in this work. Because the nitrous oxide operates on its saturation curve, its modelling may require complicated two phase flow in the feed system including the injector elements. A simplification is introduced to address this point. As shown in Figure 6, because a pressure drop is forced on the oxidizer through the injectors, it is assumed that nitrous oxide completely changes phase through the injector and across the converging pre-chamber duct it is accelerated into the fuel grain port in the gaseous state. Therefore, the pre-chamber can be considered the part of the engine in which the oxidizer is adjusted before burning into the combustion chamber; consequently, it is not considered in the computational domain. As will be clear in the following sections, the flow next to the pre-chamber exit section is similar to a confined turbulent jet of fluid discharged from a circular nozzle; a surface of discontinuity separates the main stream and the neighboring fluid, which, for the presence of the wall, generates a recirculating flow. Surrounding fluid, including the gaseous fuel coming from the wall, is entrained at the boundary and burns with the oxidizer. In this way, the jet spreads in the form of a cone having a defined angle.

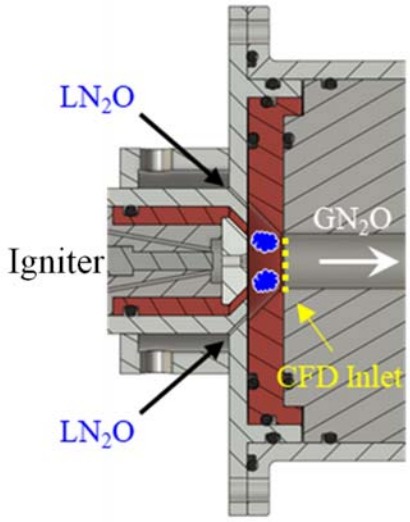

Figure 6 Schematic of the oxidizer injection arrangement.

In addition, it is worth highlighting that, differently from the case of pure gaseous oxygen, the nitrous oxide combustion mechanism with ethylene occurs following two different steps:

1. First, it decomposes into gaseous oxygen and nitrogen at the decomposition temperature of 1907 K. The position of the decomposition flame mainly depends on both the nitrous oxide injection velocity and the decomposition rate.
2. Second, the decomposition products burn with ethylene releasing combustion products at higher temperatures upwards of 2800 K. A non-premixed flame develops into the combustion chamber, which basically depends on the local mixture ratio and turbulent intensity.

By summarizing, with the specific purpose of estimating the regression rate, the problem complexity can be significantly reduced if the oxidizer conditions upon injection into the chamber, before combustion between the released oxygen and ethylene takes place, in terms of enthalpy and velocity are properly described. Therefore, although the oxidizer inlet phenomena are not described in detail, the results (as demonstrated in the next section) show that the assumptions allow for a fairly accurate evaluation of the heat transferred from the flame to the fuel grain.

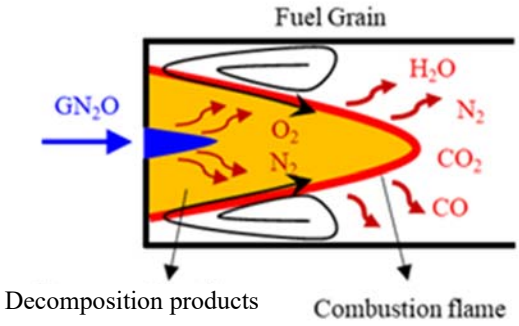

Figure 7 Combustion mechanism of nitrous oxide with ethylene.

Because the above-mentioned multispecies computational model is designed to describe non-premixed flames – i.e., no reaction mechanism is taken into account – the decomposition process cannot be considered in the CFD simulations. To overcome this issue, it is assumed that the gaseous nitrous oxide instantaneously decomposes at the grain inlet, and a molar mixture of 33.3% O2 and 66.7% N2 is enforced at a temperature equal to the decomposition temperature. The reaction mechanism is summarized in Table 4.

Table 4 Simplified scheme of nitrous oxide combustion.

Mechanism	Limiting Process	Reaction
1	Reaction Rates	$GN_2O \rightarrow N_2 + 0.5O_2$
2	Propellant Mixing	$N_2 + 0.5O_2 + C_2H_4 \rightarrow$ combustion products

The typical computational domain represents the internal volume of the fuel grain, the post-chamber, and the nozzle. On the inner surface of post-chamber, as well as on the nozzle wall, no-slip and adiabatic boundary conditions are imposed. The inlet of the computational domain coincides with the outlet section of the pre-chamber, as highlighted in Figure 6. At the injector exit section, a mass flow inlet boundary condition is prescribed, the temperature is set equal to the full decomposition temperature of nitrous oxide (1907 K), the oxygen and nitrogen molar fraction are set equal to 0.34 and 0.66, respectively, and the turbulent quantities are assigned. Finally, a pressure outlet condition is set at the nozzle exit section.

The main dimensions are listed in Table 5, and Figure 8 shows the computational grid employed in the fuel-port configuration relative to the average port diameter achieved in Test 1. A grid sensitivity analysis was carried out with three mesh refinement levels to determine the dependency of numerical results on the spatial discretization based on the configuration of Test 1. A coarser and a finer mesh are constructed starting from the reference mesh, which consists of 32,414 regular cells: they are generated respectively doubling and halving the cell size in both the axial and the radial directions (in the clustering zone the size is set only for the first layer, while the size of the subsequent layer depends on the bunching law). Figure 9 shows a log-log plot of the numerical error versus the minimum grid size for the average values of the regression rate for both engine configurations. The numerical error is calculated as the relative difference between the value obtained in the simulations (which are resumed in Table 6) and the relevant Richardson's extrapolation [44]. A satisfactory approximation of the numerical results is believed to be obtained with the reference mesh.

Table 5. Computational domain dimensions.

Grain length	Post diameter	Post Length	Nozzle length
270 mm	25.90 mm	20 mm	40 mm

Table 6 Grid sensitivity analysis results based on the computed total regression rate.

Mesh refinement	regression rate, mm/s
Coarser	0.390
Reference	0.370
Finer	0.362

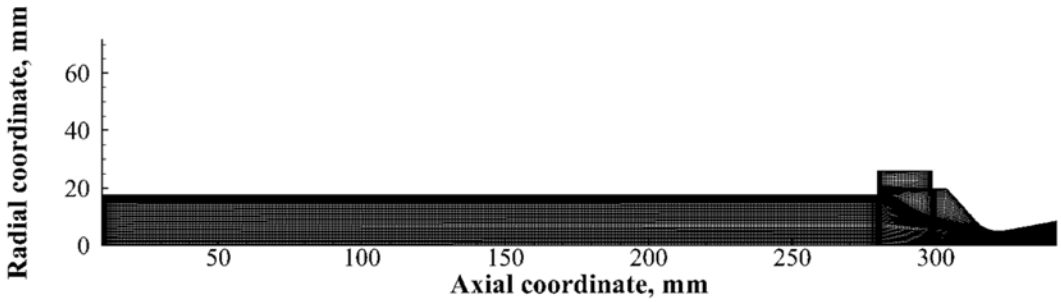

Figure 8 Computational grid.

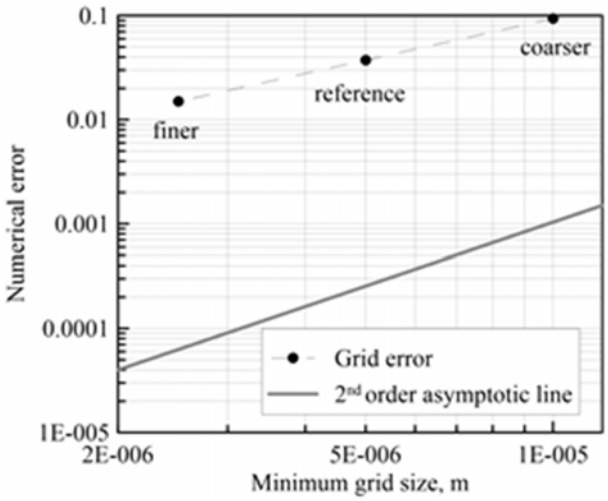

Figure 9 Numerical error versus grid size.

3.4. Transient Solution Procedure

A transient quasi-steady solution is adopted in order to make the overall numerical model fully predictive without the need of data, e.g. the time-space-averaged grain diameter from experimental tests. The method also allows an in-depth validation of the numerical model as well as a critique of the simulations performed at the time-space average grain port diameter. The numerical burden is drastically reduced by assuming that the fluid dynamic characteristic time is much shorter than the time required for the thermal profile adjustment in the solid grain due to a change in the port diameter. In this framework, the temporal advancement of the grain diameter can be simulated by a series of steady-state simulations. Once computed the nodal regression rate along the grain surface, the diameter is updated by means of:

$$\Delta_i^n = \dot{r}^n(x_i)\Delta t \tag{28}$$

where Δ_i^n is the cell centroid displacement and $\dot{r}^n$ is the local regression rate at the n-th time-step. The Δt used in the simulation is of 10 s. The simulations are carried out at each time-step starting from the time zero until the test end.

Noting that the grain diameter is not constant along the axis, the local displacement may include an axial component in addition to a radial one. Denoting the local inclination of the i-th cell face on fuel surface with respect to the axial direction with θ_i^n (see Figure 10), the coordinates of the face centre at the n+1-th time-step are calculated as:

$$x_i^{n+1} = x_i^n - \Delta_i^n \sin\theta_i^n \tag{29}$$

$$y_i^{n+1} = y_i^n + \Delta_i^n \cos\theta_i^n \tag{30}$$

from which the updated local port diameter is, $D_i^{n+1} = D_i^n + 2\Delta_i^n \cos\theta_i^n$. The fluid domain geometry is modified accordingly, and a new computational mesh is generated; a steady-state numerical simulation at the new time-step n+1 is, then, performed.

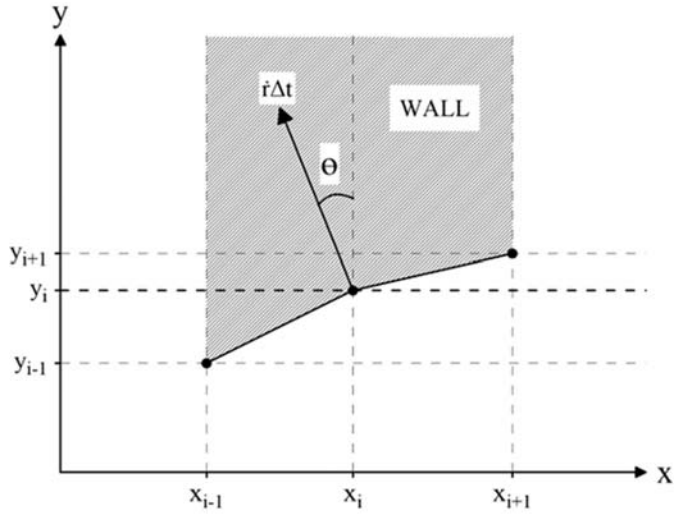

Figure 10 Schematic representation of the i-th node displacement components.

3.5. Regression Rate Reconstruction Technique

The reconstruction method used in this work was first presented in Ref. [45]. Assuming quasi-steady operation, the rocket thrust can be expressed as:

$$F = \dot{m}' v_e' c_d \lambda + (p_e - p_a) A_e \tag{31}$$

where $\dot{m}'$ is the isentropic one-dimensional mass flow rate through the nozzle computed at the chamber conditions, v_e' is the isentropic one-dimensional exit velocity, $\lambda \approx 0.997$ is the momentum-thrust reduction factor, which takes into account the thrust loss for the divergence of the rocket nozzle, c_d is the discharge coefficient which accounts for both non-one-dimensionality and non-isentropicity of the flow, p_a is the ambient pressure, p_e is the exit pressure and A_e is the nozzle exit section area.

Dividing both sides of Eq. (31) by the chamber pressure and the throat area, one can obtain:

$$\frac{F}{p_c A_t} = \frac{v_e'}{c_{th}^*}\frac{c_d \lambda}{\eta} + \left(\frac{p_e}{p_c} - \frac{p_a}{p_c}\right)\frac{A_e}{A_t} \tag{32}$$

where $\eta = \frac{c_{exp}^*}{c_{th}^*}$ is an efficiency coefficient which corrects the theoretical characteristic velocity to obtain the experimental one. Thrust and pressure appearing in Eq. (32) are quantities known from the experimental tests and they are function of time, whereas the exit velocity, the exit pressure and the theoretical characteristic velocity are computed with the software CEA [39] imposing at all time steps the experimentally measured chamber pressure and oxidizer to fuel ratio *OF*. This latter is calculated from the steady state expression of the mass balance equation:

$$c_{th}^{*}\left[\left(1+OF\right)/OF\right]-\frac{p_c A_t}{\eta \dot{m}_{ox}}=0 \tag{33}$$

Note that, because the oxidizer mass flow rate is evaluated as time derivative of the tanks weight during the burning time, the instantaneous $\dot{m}_{ox}$ is hard to be evaluated. The mass flow rate can be assumed constant during the burning time in Test 1, but this is not true in Test 2, indeed it decreases during the tanks' emptying. However, because the emptying time is low with respect to the overall burning time, the inaccuracy produced by the assumption of constant mass flow rate is assumed negligible. In addition, the purpose of the current analysis is to investigate the trend of the regression rate during the burning time rather than the exact instantaneous value.

Once computed the spatially averaged OF at the i-th timestep, the space-averaged regression rate and the updated grain diameter can be obtained as:

$$\dot{r}=\frac{\dot{m}_{ox}}{OF}\frac{1}{\rho_s \pi D_i L} \tag{34}$$

$$D_{i+1}=D_i+2\dot{r}_i\,\Delta t \tag{35}$$

where the time-step considered is equal to the data sampling time of 10 ms. An additional equation is needed for the computation of the discharge coefficient. This quantity is calculated by requiring that the computed total fuel mass, $\Delta M_f'$, consumed during the burning is equal to the experimental one, ΔM_f:

$$\Delta M_f'(c_d)-\Delta M_f=0 \tag{36}$$

Figure 11 shows the characteristic velocity, exhaust velocity and exit pressure as functions of the mixture ratio in the conditions typical of the tests analysed here. The curves have been obtained with the CEA software by inputting a fuel with chemical formula C_2H_4 and formation enthalpy of -53.170 kJ/mol at the temperature of 293 K and pressure 12 bar.

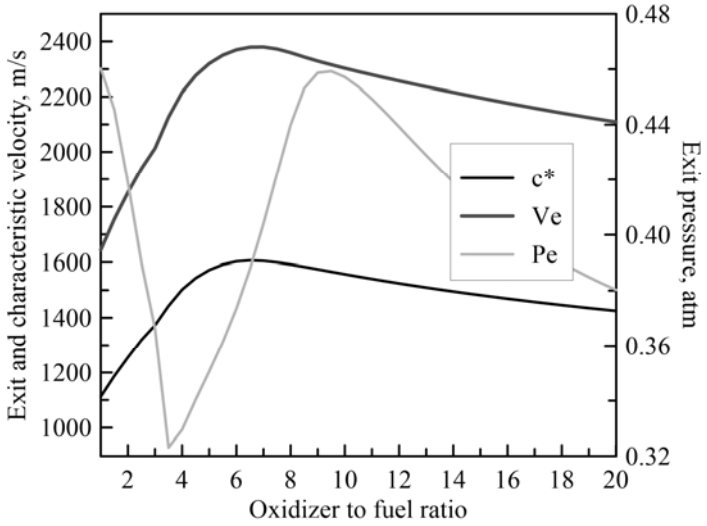

Figure 11 Characteristic velocity, nozzle exit velocity and exit pressure as functions of the mixture ratio at the operating pressure of 13 bar.

The adopted calculation procedure is the following:

1) An arbitrary discharge coefficient is imposed;

2) η and *OF* are calculated by means of Eqs. (32) and (36), respectively, by an iterative process (since c_{th}^{*} is a function of *OF* and evaluated by CEA).

3) The instantaneous spatially averaged regression rate is computed, and the grain diameter is updated.

Points 2) and 3) are repeated at each time-step until the extinguishment of the test. Eq. (36) is checked and if a suitable convergence criterion is not satisfied, the discharge coefficient is recomputed according to the bisection method.

4. Results and Discussion

In this section, the results obtained with the numerical model presented above are shown. First, they are compared with the experimental data. Some discrepancies in the average data are also investigated by means of transient procedures. Second, the effect of the inlet temperature on the regression rate is studied to understand the reliability of the assumptions described above. Then, the same results are compared with those obtained with either oxygen or 85wt% hydrogen peroxide. Finally, a different pre-chamber arrangement is suggested to mitigate the issues appearing in the current configuration.

4.1. Numerical Model Validation

The experimental tests described in Subsection 2 have been used as a benchmark for the assessment of the CFD model. The time averaged oxidizer mass flow rates listed in Table 1 were enforced in the simulations. For the sake of clarity, note that a molar mixture of 34% oxygen and 66% nitrogen at the decomposition temperature of 1907 K is set at the inlet.

Figure 12 displays the temperature contours obtained at the average port diameter of Test 1 with the relative velocity streamlines. The pre-chamber arrangement produces an axial round jet of the oxidizer flowing into the combustion port, which, as anticipated above, leads to the creation of a recirculating fluid zone establishing, on a time-averaged basis, as a separated, toroidally-shaped region with and eddy-like structure wherein back-flowing currents transport mass, energy, and momentum from downstream toward the combustion-chamber inlet section. This toroidal, large vorticity region with high levels of turbulent intensity and relatively low average velocities generates a wall heat flux enhancement with a peak nearly corresponding to the point of impingement on the grain surface of the injected gas. In-depth studies regarding the effect of the recirculation zone on the fuel regression rate are available in Refs. [11, 29].

Figure 13 displays a comparison of the regression rate profiles calculated along the grain length at the average port diameter with the experimental data points. It is clearly shown that the current model well predicts the behavior of the regression rate, with particular reference to the position of the regression rate peak, which is roughly located at around 90 mm in both test cases. Table 7 displays a comparison of the time-space averaged regression rate in the two tests: the deviations from the experimental values are about 12% and 3% for Test 1 and 2, respectively. The reason for this mismatch is explained in the next subsection. In addition, the computed characteristic velocities are 1442 and 1461 m/s in Test 1 and Test 2, respectively. However, it is worth noting that comparison with the experimental data is not meaningful, for the difference between the computed and measured regression rates which imply different mixture ratios.

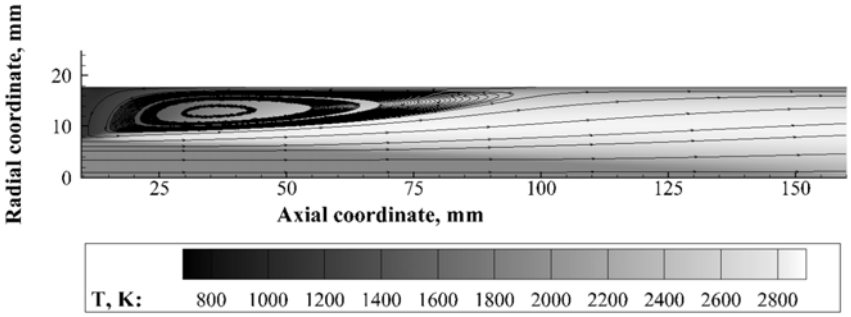

Figure 12 Temperature contour plot with overlapped streamlines of Test 1.

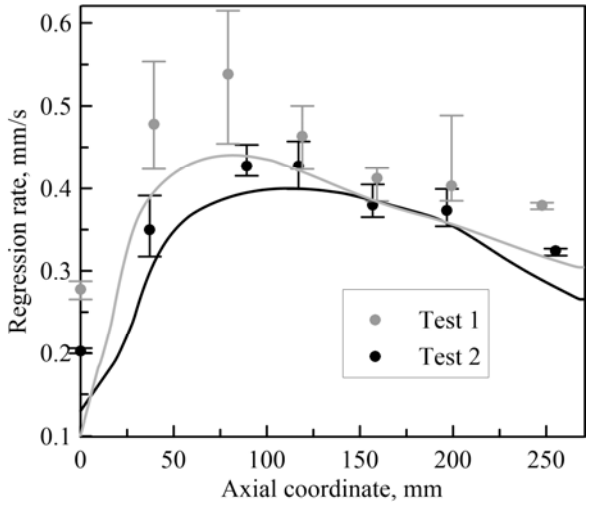

Figure 13 Comparison between measured and calculated regression rate.

Table 7. Measured vs calculated regression rates.

Test	Experimental, mm/s	Numerical, mm/s	Error, %
1	0.422* ± 0.021 (0.467** ± 0.11)	0.370	12.3 (20.8)
2	0.355* ± 0.014 (0.401** ± 0.08)	0.344	3.1 (14.2)

4.2. Transient Model Validation

The results presented above can just provide a partial validation of the current model, for a full understanding of the reliability of which, a further validation was performed in transient conditions by comparing the ballistically reconstructed spatially-average regression rate over time (obtained as described in Subsection 3.5) with the one numerically calculated with the procedure described in Subsection 3.4. The main purpose of this comparison is analysing the major deviation between the computed and measured regression rates in Test 1 and the fair match between the two achieved in Test 2. Constant mass flow rate is enforced in both the simulations despite it drops at the end of the Test 2 for the reasons expressed above. However, the

comparison of the computed regression rate with the reconstructed one is still valid in Test 2, because a constant mass flow rate was also enforced in the reconstruction technique. In addition, the purpose of the current analysis is the understanding of the deviation of the computed regression rate from the experimental one in Test 1 and, on the other hand, the good match achieved in Test 2. Figure 14a depicts a comparison of the four regression rate time trends obtained by means of the described reconstruction technique and CFD simulations: two for Test 1 and two for Test 2. Note that the difference of about 5% between the oxidizer mass flow rates imposed in the CFD simulations in Test 1 and Test 2 does not produce evident changes in the regression rates, therefore, the two CFD curves appear as mostly overlapped with each other. The CFD curves follow the ballistically reconstructed data except over the first ten seconds of operation, which is the phase when the igniter was on. In this time frame, the reconstructed regression rate in both tests is over 1 mm/s, which is unusually large for plastic fuels, and it is about the double of that predicted by CFD, which is around 0.7 mm/s. Therefore, on the one hand, it is likely that the deviation of the computed regression rate from that measured in Test 1 (12.3% in Table 5) is mainly due to the influence of the ignition system, which produces the anomalous initial regression rate enhancement. Indeed, as mentioned above, the ignition system consists of a miniaturized hybrid rocket, which directly exhausts hot combustion gases in the rocket chamber. On the other hand, looking at the comparison with the reconstructed data in Test 2, it can be clearly seen that, while the same deviation is present over the first instants of the firing, for the much longer duration, a large regression rate decrease is reconstructed at the end of the firing test, corresponding to the emptying of the oxidizer tanks. Hence, the positive and negative deviations seen at the beginning and at the end of the test tend to counterbalance each other, explaining the relatively low error between numerical and experimental average regression rate in Test 2: the initial regression rate augmentation is compensated by the final regression rate decrease due to the reduced oxidizer mass flow rate to the chamber. The authors would like to highlight that the reconstructed regression rate in this test is not rigorous, because the oxidizer mass flow rate is surely not constant at the end of the test. However, the comparison with the CFD simulations is still valid because the same mass flow rate was enforced in both the analyses.

Further observations can be made with the aid of Figure 14b, which shows the comparison of the calculated and reconstructed regression rates over time as function of the corresponding oxidizer mass fluxes. The engine operates in the range of 15-40 kg/m^{2}s oxidizer mass fluxes for about 85% of the overall burning time, and for only 15% of the time at mass fluxes higher than 100 kg/m^{2}s, in the beginning of the firing. Thus, the grain port enlargement is characterized by a rapid initial rate followed by an approximately constant increase of the diameter (constant regression rate). As discussed with reference to Figure 14a, the regression rate curves obtained with CFD yield large deviations from the experimentally reconstructed curves both up to 10 s and roughly from 60 to 70 s. Outside those time intervals, the computational and ballistically reconstructed data are fairly overlapped, which suggests that the numerical model is able to predict the fuel grain consumption.

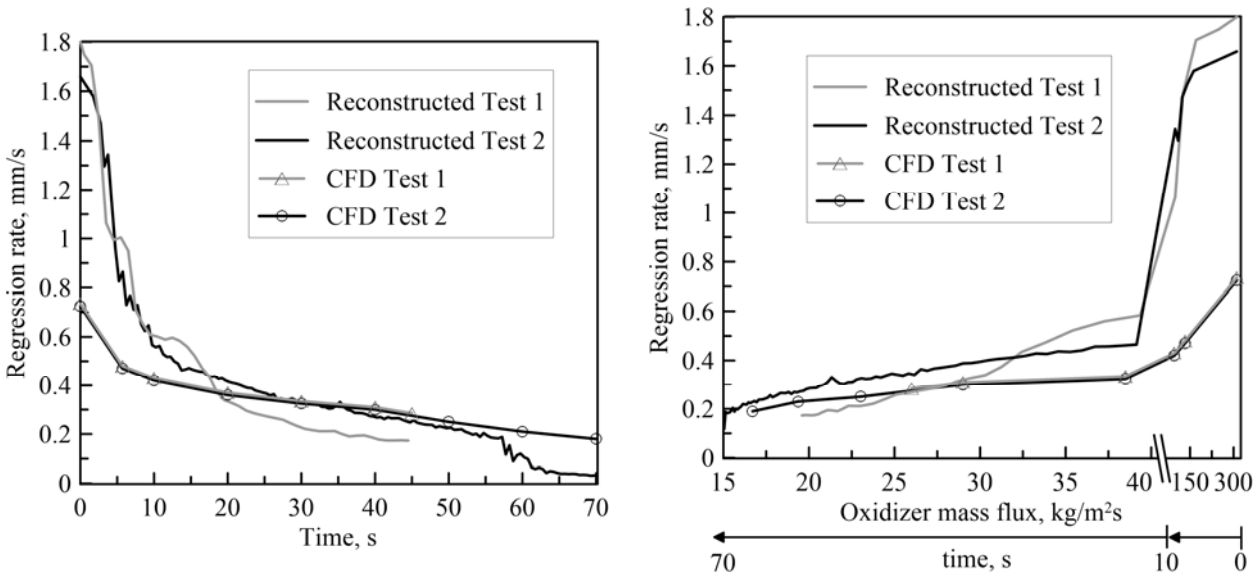

(a). **(b).**

Figure 14. Comparison of the experimentally reconstructed and numerically calculated regression rates, a) as a function of time, b) as a function of the oxidizer mass flux.

The regression rate dynamics discussed above can be explained by observing the time evolution of the internal flow field with the aid of the temperature contour plots displayed in Figure 15. The growth over time of the recirculation-zone extension in the grain port can be clearly recognized, so that the two regression-rate evolution phases can be ideally distinguished. At the beginning of the firing, say up to 10 seconds in the burn, the recirculation bubble is confined to the inlet of the combustion port, and its effect on the space-averaged regression rate is negligible; regression rate, thus, is expected to decrease with time with the oxidizer mass flux according to well-known Marxman's correlation, $\dot{r} \propto D^{-2n}$, in which n is the exponent of the oxidizer mass flux. Later on in the firing, as the extension of the flow recirculation in the port is raised, the effect tends to become significant, leading to an augmentation of the regression rate. Flow recirculation promotes the mixing of propellants, and increases the local wall heat flux compared to the one that would be obtained in the absence of recirculation itself, which mitigates the regression rate decrease due to the port enlargement and the consequent mass flux reduction.

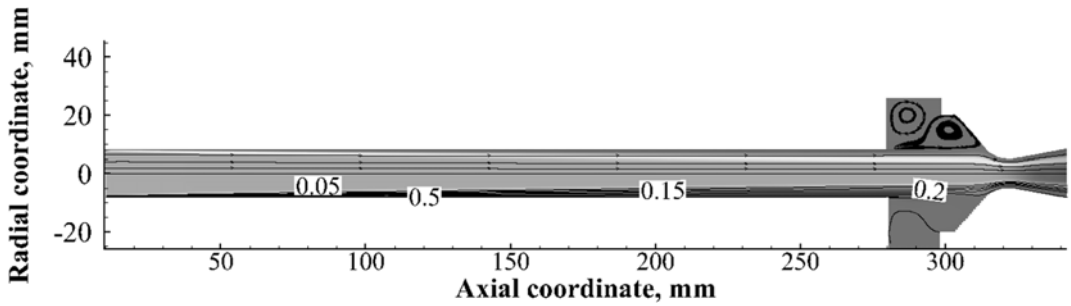

t = 0 s

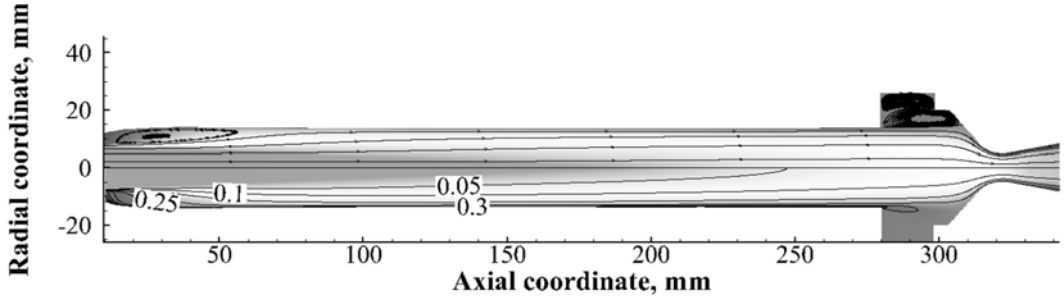

t = 10 s

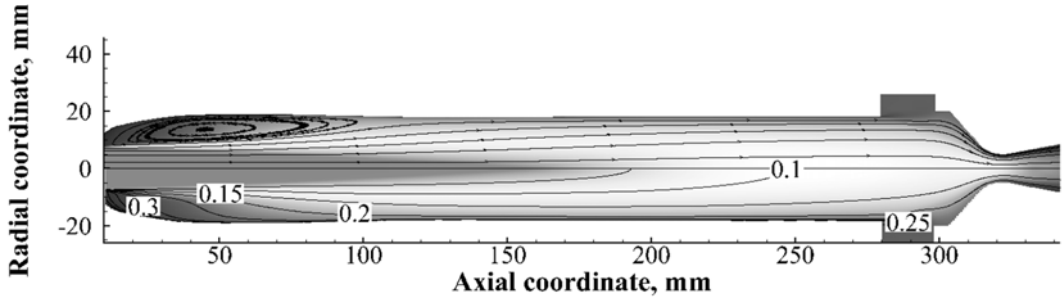

t = 20 s

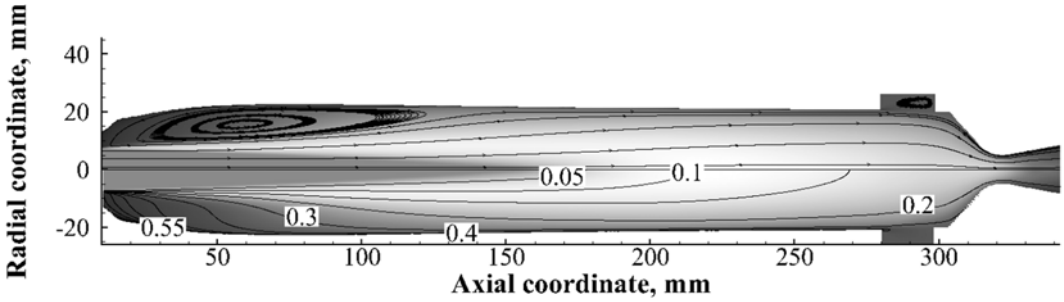

t = 30 s

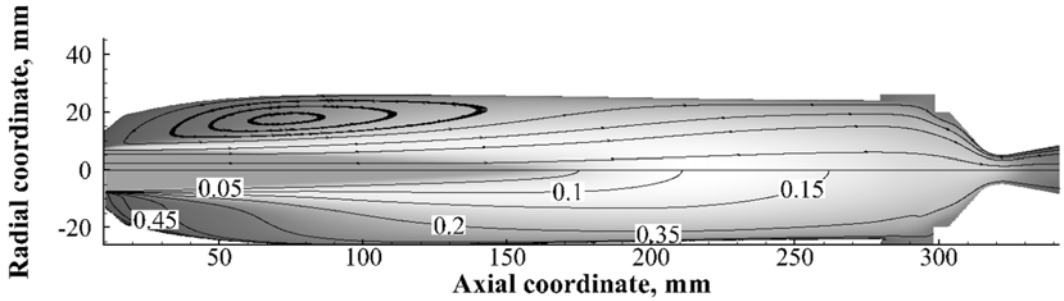

t = 40 s

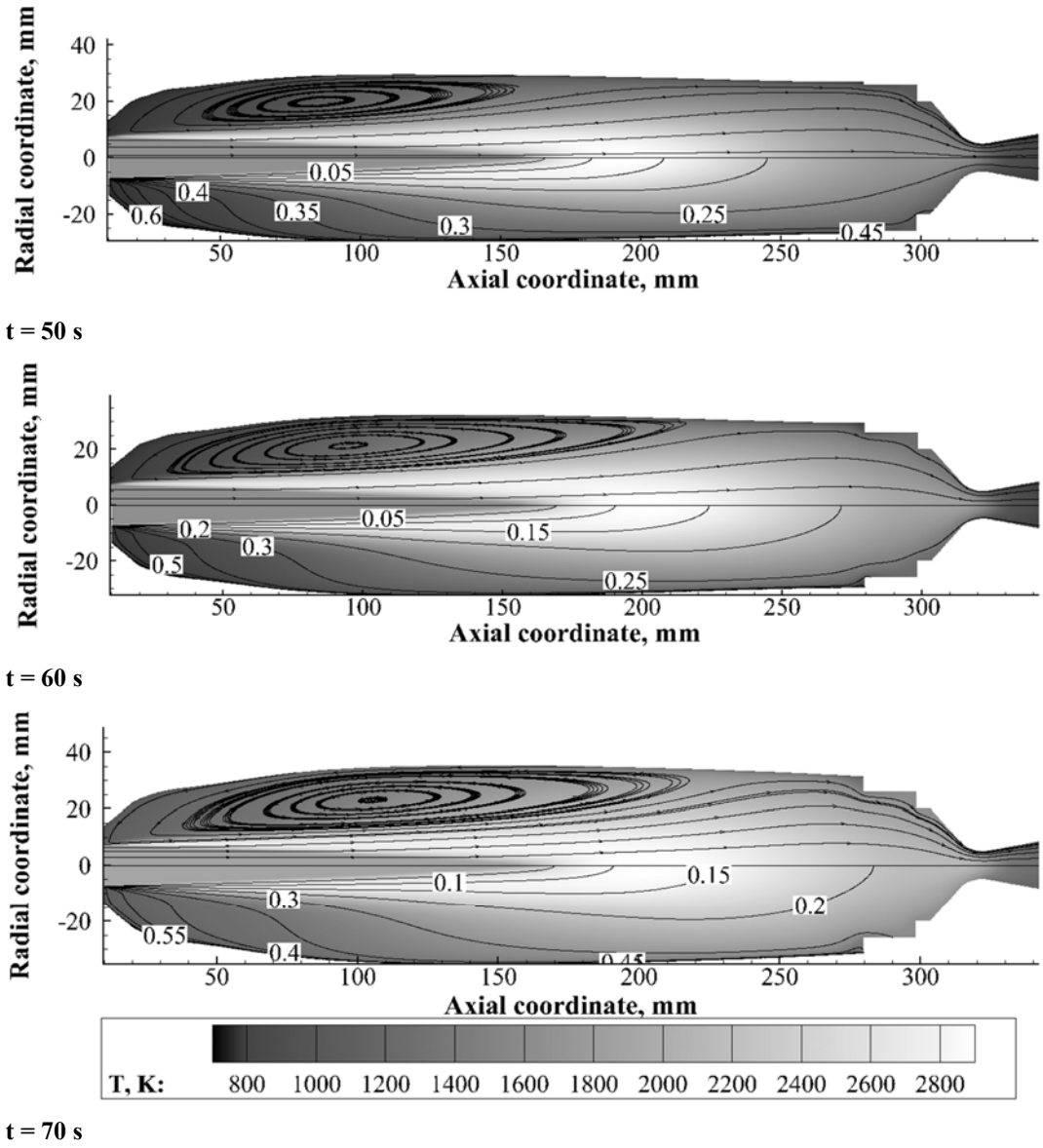

Figure 15 Temperature contour plot with overlapped streamlines (top half) and mixture fraction iso-lines (bottom half).

The inlet jet spreading angle is estimated to be around 5.6 degrees and it appears constant during the burning time. Hence, the bubble extension linearly increases with the grain diameter. Figure 16 displays the evolution of the regression rate spatial profiles during the burning: each profile corresponds to the related flow field shown in Figure 15. According to the discussion above, at t = 0 s, regression rate slightly increases along the grain length because no recirculating zone is present into the chamber; in the later phases, the effect of the recirculating zone increases and, at t = 10 s, it is confined to 70 millimetres down the port; as time increases, the grain portion affected by the presence of the recirculation further extends and this effect becomes predominant.

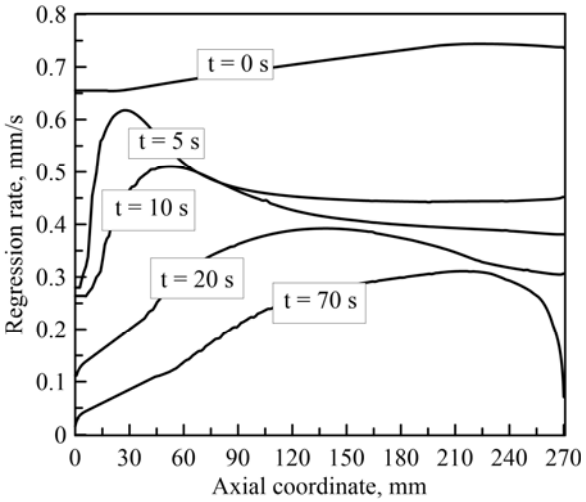

Figure 16 Regression rate axial profiles over time.

Figure 17 displays the comparison between the measured final grain diameter profile of Test 2 and the numerical profile rebuilt by the CFD transient procedure. A good match is shown with a reliable prediction of the point featuring the largest fuel consumption.

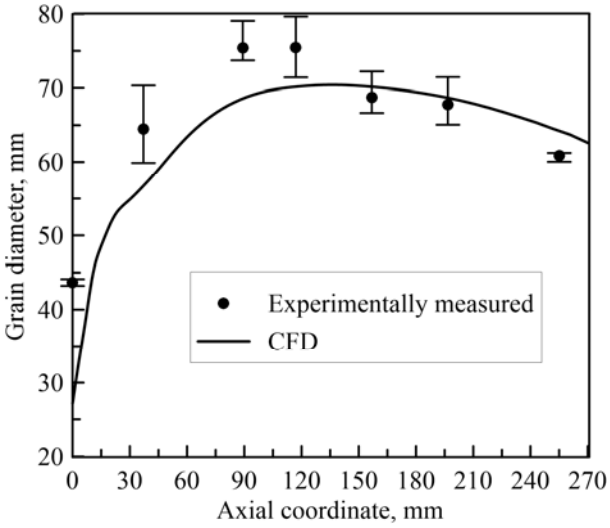

Figure 17 Comparison of the experimentally measured and calculated final grain diameter profile in Test 2.

Excluding the first 10 s, a simplified equation expressing the regression rate as a function of time is provided in Figure 18. This latter, from a practical point of view, allows estimating the spatially averaged regression rate, once the burning time is given, as follows:

$$\bar{\dot{r}} = -0.0035t + 0.4391 \tag{37}$$

where the regression rate is expressed in mm/s and time in seconds. An increase of around 15% is suggested to take into account the effect of the ignition system. Then, the average grain diameter can be computed by $\overline{D} = (D_1 + 2\bar{\dot{r}}t)/2$ and a CFD simulation can be performed to detect the most critical point in terms of fuel consumption. In this way, the numerical cost required by the transient procedure can be avoided.

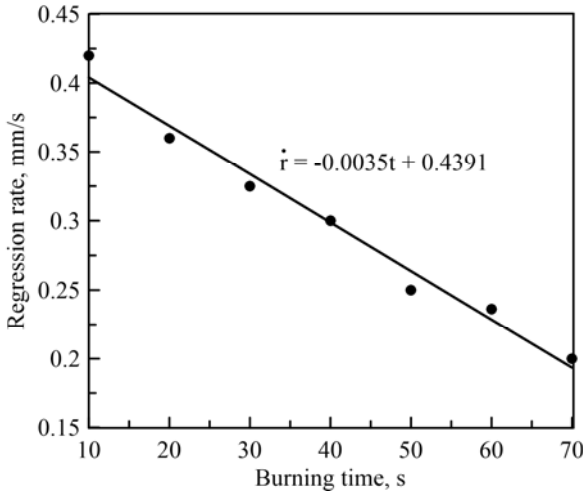

Figure 18 Calculated spatially averaged regression rate over time.

4.3.Effect of the Inlet Temperature

In this section, the effect of the oxidizer inlet temperature on the regression rate is investigated to assess the accuracy of the assumptions made above. A series of numerical simulations have been carried out by arbitrarily imposing the inlet temperature; note that, assuming an inlet temperature lower than the one relative to the nitrous oxide complete decomposition would, in principle, involve different inlet mixtures including non-dissociated N2O with O2 and N2. Nonetheless, here the complete decomposition mixture (made of 34% oxygen and 66% nitrogen) is maintained in all the simulations, which, as shown in the following, produces negligible effects on the resulting regression rate.

Figure 19a displays the regression rate axial profiles calculated with 4 different inlet temperatures (ranging down to the extreme of 500 K) at the average port diameter of Test 1. It is worth pointing out that inlet temperatures larger than 1907 K are not realistic, as this latter is the temperature reached with the gaseous nitrous oxide complete decomposition. This parameter has significant effect on the results both in terms of the axial profile and average regression rate value. In fact, with the inlet temperature of 500 K, the calculated regression rate is nearly constant down the grain length and its average value is around 0.16 mm/s, i.e., half of that obtained with 1907 K. Thus, by imposing temperatures lower than 1907 K, the computed fuel consumption profile tends to deviate from the one experimentally observed.

The inlet temperature also affects the wall shear stress profile. In fact, the point of zero shear stress on the fuel grain tends to move downstream as the inlet gas temperature increases. The overall effect is such that, if one estimates the spreading angle, α, of the oxidizer jet into the combustion chamber as follows:

$$\alpha = tan^{-1}\left[\left(D - D_{pre}\right)/L_r\right] \tag{38}$$

where D_{pre} is the diameter of the prechamber exit section (i.e., the one adjacent to the grain inlet port) and L_r is the length of the recirculation zone (i.e., the grain portion enclosed between the inlet section and the point of zero-shear stress), it would decrease with temperature.

In particular, the spreading angle linearly decreases with the inlet temperature as shown in Figure 19b. Higher inlet temperature involves higher inlet velocity and, in turn, larger momentum flux of the incoming oxidizer flow (the oxidizer mass flux being unchanged); therefore, the effect is to move the impingement point forward on the fuel grain. From Figure

19b, the angle extrapolated down to 300 K is around 6.6 degrees, which is actually lower than that computed in previous works with gaseous oxygen (which is around 9 degrees [11, 13]). Because an increased inlet temperature involves enhanced regression rate (for the increased heat flux to the wall), the influence of the latter on the jet spreading angle is also studied, with the aim of looking into the contributions of the temperature itself and of the augmented regression rate on the angle variation. Figure 20 displays a comparison of the wall shear stress profiles evaluated with the same temperature of 1907 K and either the resulting regression rate (whose average value is equal to 0.37 mm/s) or the imposed constant regression rate of 0.1 mm/s. As expected, for the lower entrainment of fuel into the main stream, the effect of the lower regression rate is to further reduce the jet spreading angle from 5.6 to 5.2 degrees. Hence, the conclusion is that larger inlet temperature involves smaller jet spreading into the grain port despite the increased fuel regression, due to the flow acceleration.

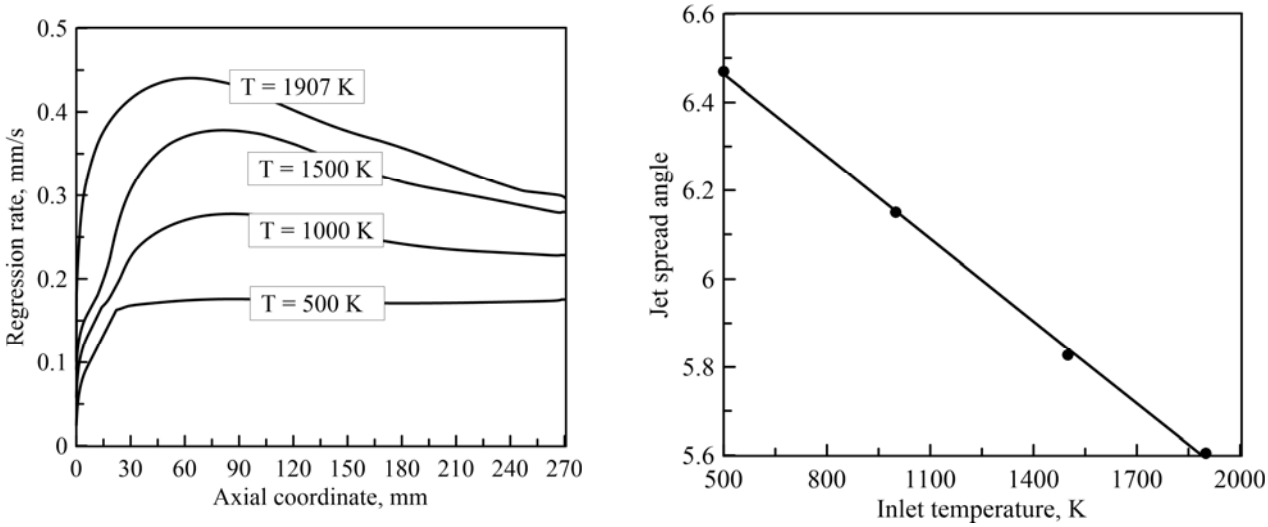

(a) **(b)**

Figure 19 a) Regression rate axial profile and b) jet spreading angle calculated in Test 1 by varying the inlet temperature.

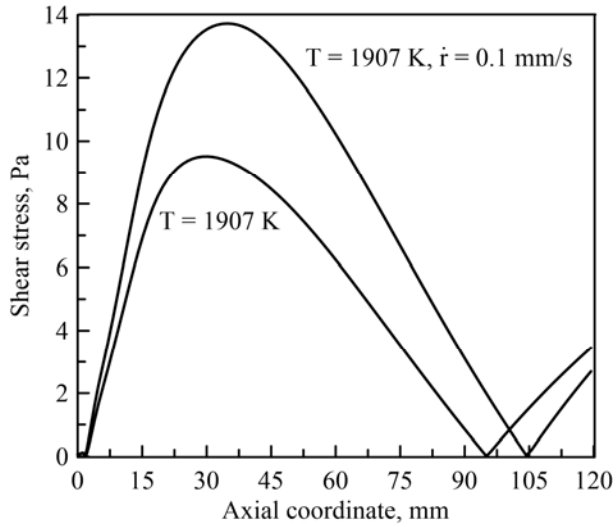

Figure 20 Axial shear stress profiles obtained with an inlet temperature of 1907 K and either calculated or imposed regression rate.

With reference to the influence of the nitrous-oxide decomposition mixture on the results, consider Figure 21, which displays the comparison of the equilibrium combustion temperatures (recall that, in the current CFD model, combustion is assumed to occur in equilibrium) calculated at the inlet temperature of 1500 K with both the fully and partially dissociated nitrous-oxide mixture burning with polyethylene. Over the whole considered range of mixture ratios, considering the gas mixture deriving from the complete decomposition of N2O, instead of the actual one corresponding to 1500 K, causes an underestimation of the combustion temperature from 5% up to 7%. However, by changing the temperature from 1907 K to 1500 K (i.e., of about 20%), regression rate decreases by 20% (see Figure 19a); thus, as expected, the main parameter affecting the regression rate is the inlet temperature, regardless of the composition of the inlet oxidizer stream.

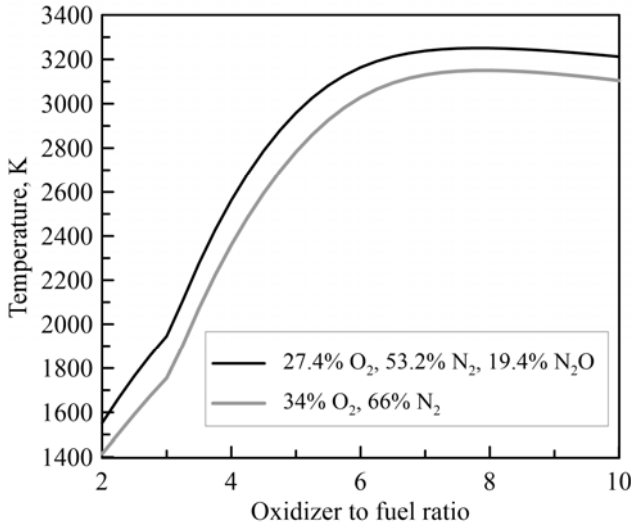

Figure 21 Equilibrium combustion temperature calculated at 1500 K inlet temperature with either completely or partially decomposed N2O burning with polyethylene.

4.4.The cases of Oxygen and Hydrogen Peroxide

In this section, the previous results are compared with those obtained using either pure gaseous oxygen or 85wt% hydrogen peroxide at equal mass flow rates. According to the above-mentioned simplifications, a mixture of 73% H_2O and 27% O_2 molar fractions with a dissociation temperature of 1753 K is set up for the latter case. The considered reaction mechanism is given here:

$$0.75H_2O_2 + 0.25H_2O \rightarrow 0.73H_2O + 0.27O_2$$

Pure oxygen is injected with the temperature of 300 K. Figure 22 displays a comparison of the regression rate profiles calculated in the conditions of Test 1 and Test 2. As clearly shown, the average values and the shape of the regression rate profiles are mostly similar in the cases of hydrogen peroxide and nitrous oxide, whereas both these latter are different from the case of the gaseous oxygen in which the predicted average value is roughly half of the one obtained with the other oxidizers and the regression rate peak is located significantly upstream (i.e., at around 30 mm from the fuel grain leading edge against 90 mm). All the results are summarized in Table 8.

Table 8. Summary of the regression rates obtained with different oxidizers in the two tests.

	Test 1 $\dot{r}$, mm/s	Test 2 $\dot{r}$, mm/s
N_2O	0.37	0.34
85wt% H_2O_2	0.38	0.35
O_2	0.21	0.19

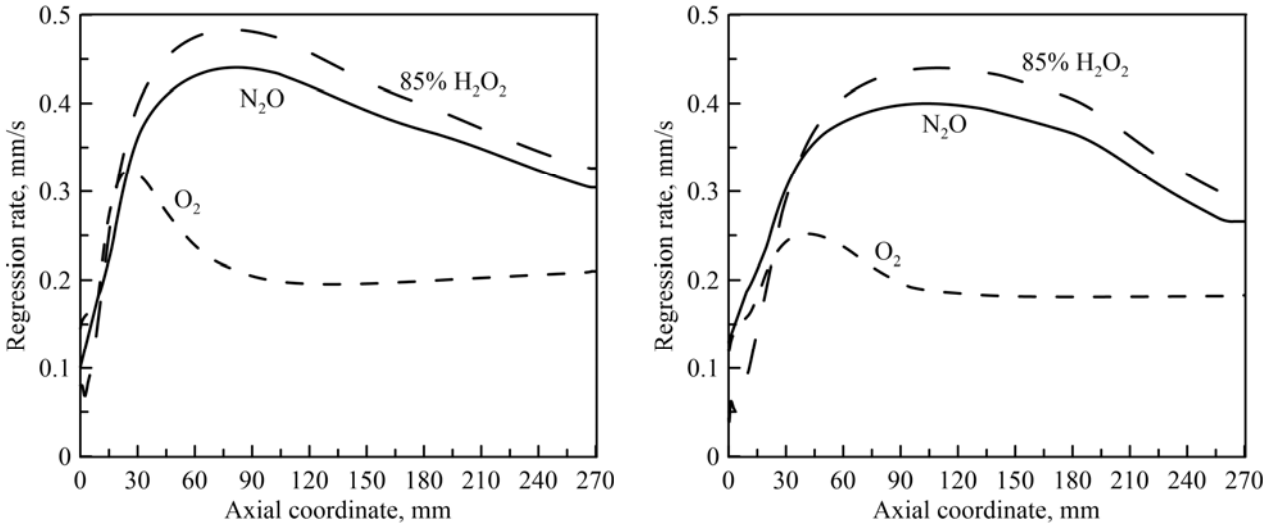

(a) Test 1. **(b) Test 2.**

Figure 22 Comparison of the regression rate profiles predicted with nitrous oxide, 85wt% hydrogen peroxide and pure oxygen.

The lower regression rate calculated with oxygen, based on the arguments explained in the following, does not have to be surprising. Furthermore, experimental data available in the literature are largely scattered demonstrating that, with a given

fuel, there is no definitive trend with several oxidizers. In particular, a discussion on several propellant combinations is addressed in Ref. [46], in which data gathered with nitrous oxide and oxygen burned with HTPB show equal regression rates.

Figure 23 displays the temperature contours obtained by considering the three oxidizers in the conditions of Test 2. Under equal mass fluxes over the three cases, the main difference is represented by the extension of the recirculation zone and the temperature field. The case with pure oxygen shows the shortest recirculation extension with a low mixing degree of the fuel with the oxidizer and a relatively cold combustion chamber. The thermal decomposition occurring with both the nitrous oxide and hydrogen peroxide favors the decrease of density and an increase of flow velocity. The inlet velocity is a key parameter: a high inlet velocity increases the width of the recirculation zone and, as a result, improves propellant mixing, raising the combustion temperature and efficiency. However, it is worth pointing out that this is not always true. Indeed, an extremely high inlet velocity can also have drawbacks, as it would lead to low propellant residence time through the combustion chamber (with a given chamber volume), resulting in poor combustion efficiency.

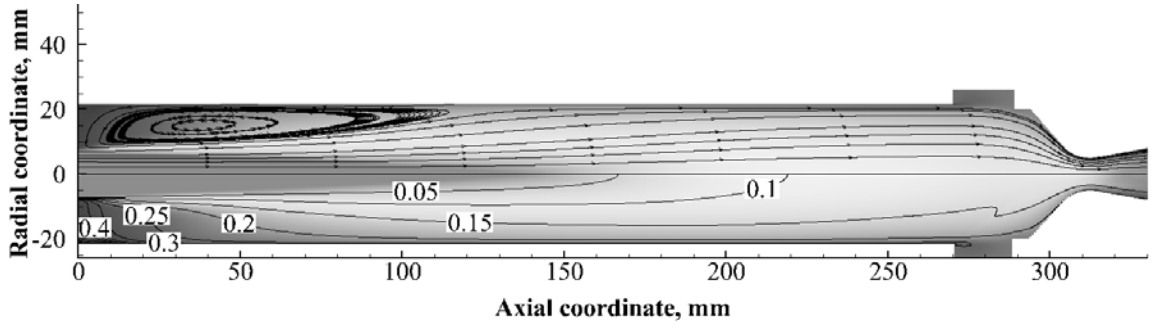

a) Nitrous oxide.

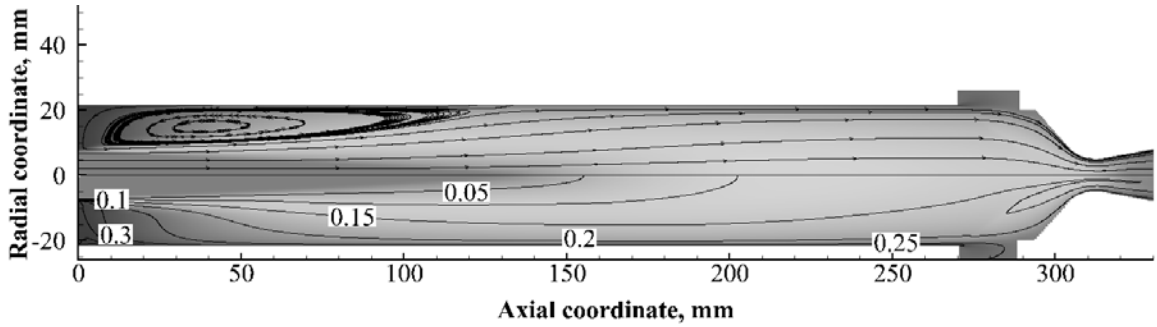

b) Hydrogen peroxide 85wt%.

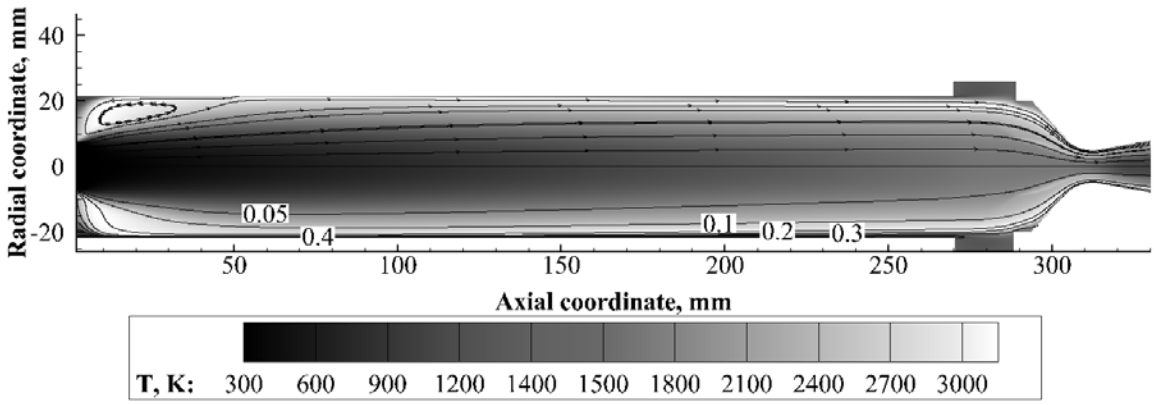

c) Oxygen.

Figure 23 Temperature contour plots with overlapped streamlines (top half) and mixture fraction iso-lines (bottom half) for the three considered oxidizers in Test 2.

Figure 24 displays the temperature and the axial velocity profiles along the vertical line placed at the middle of the grain length. Although the oxygen case shows a hotter flame that is closer to the grain surface than the other two oxidizers, the regression rate is the lowest because of the reduced convective heat transfer due to the slow fluid velocity developed in the chamber. The hot decomposition of the other oxidizers produces a strong fluid expansion leading to an enhancement of the convective heat transfer. Finally, it can be noted that the average velocity (and regression rate) of the hydrogen peroxide is slightly higher than that of nitrous oxide despite the lower decomposition temperature, because of the lighter molecular weight (34 g/mol of H_2O_2 vs 44 g/mol of N_2O).

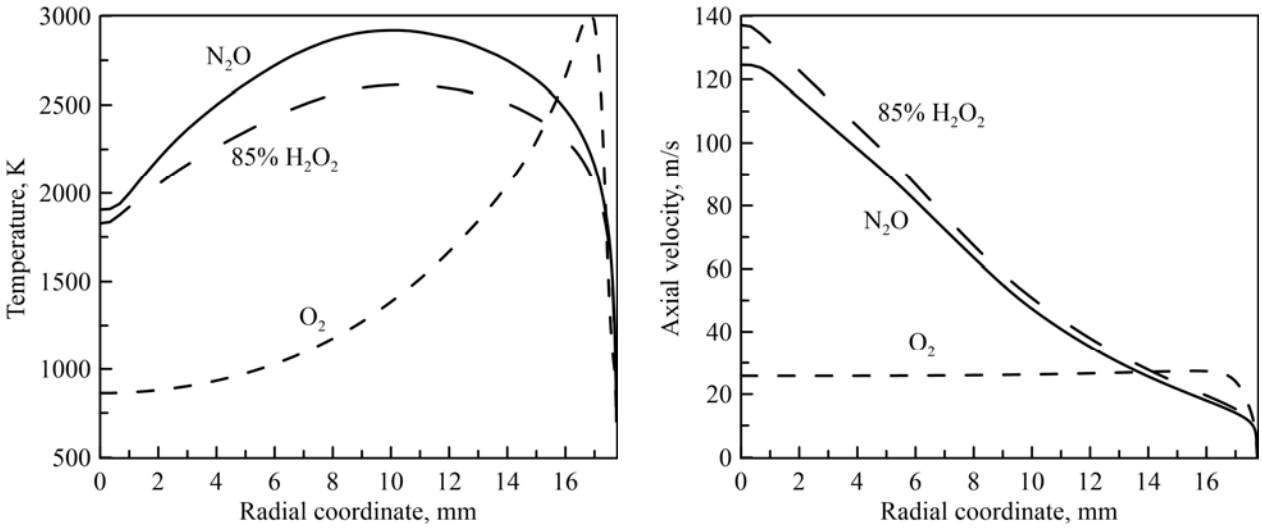

(a) Temperature radial profile. **(b) Axial velocity radial profile.**

Figure 24 Comparison of the temperature and velocity radial profiles among the three oxidizers at the middle of the grain length.

4.5. Improvement of the Prechamber Configuration

As a sort of exercise to validate the model and the concepts addressed above, a different prechamber configuration, which is here called “new”, is considered, in order to improve the engine design with the specific purpose of reducing the spatial non-uniformity of the fuel consumption. Recall that one key target of the paper was the prediction of the largest regression rate region along the grain. Figure 25 displays, again in terms of the temperature field and velocity streamlines, the results obtained with a possible alternative to the current prechamber arrangement based on previous studies [11, 12]. Assuming that the injection system evenly supplies the oxidizer in a large dump plenum upstream of the grain port inlet section (i.e., there is no jet developing in the port), no recirculation zone is involved in the chamber and the flow field is near to be one-dimensional, except at the grain leading edge where there is a confined vena-contracta (whose extension can be seen up to about 50 mm). As a result, Figure 26 displays the comparison of the regression rate computed in this arrangement with the one relative to the actual engine configuration. The regression rate profile (dashed line) appears approximately constant to around 0.2 mm/s, which is significantly reduced compared to the one obtained in the current configuration for the lower heat transfer to the wall (due to the absence of the jet impingement on the wall).

Despite the fact that the use of such a device, instead of an axial injection of the oxidizer, may appear as contradictory with respect to the wide literature claiming the benefits of the latter configuration, note that, depending on the particular engine application, performance indexes can be different. In fact, the larger regression rate along with the increased combustion efficiency and stability, all ensuing from the flow recirculation provided by the injector, can be reviewed as follows, respectively. High regression rate is not necessarily required when the engine does not have to provide large thrust. In case long firing times are involved, the significant enlargement of the fuel grain port leads to low velocities and large residence time of the gas through the combustion chamber resulting in improved combustion efficiency, which, however, in the early phase of burning, when the velocity can be high, is promoted thanks to the splitter placed in the post-chamber, (see Figure 1). Finally, although the tendency to combustion stability is, in principle, not favoured, nothing can be said about the actual behaviour of the engine deriving from the flowfield displayed in Figure 25, which depends on several aspects that need dedicated investigations.

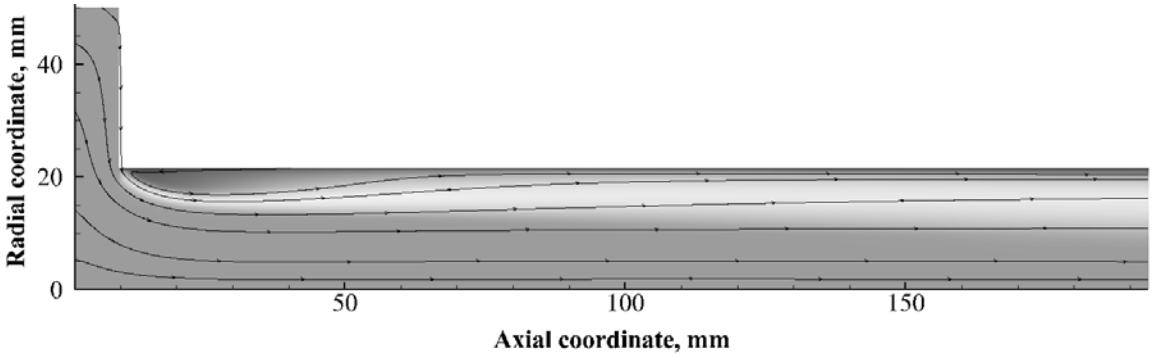

Figure 25 Temperature contour calculated in the Test 2 conditions with the new prechamber arrangement.

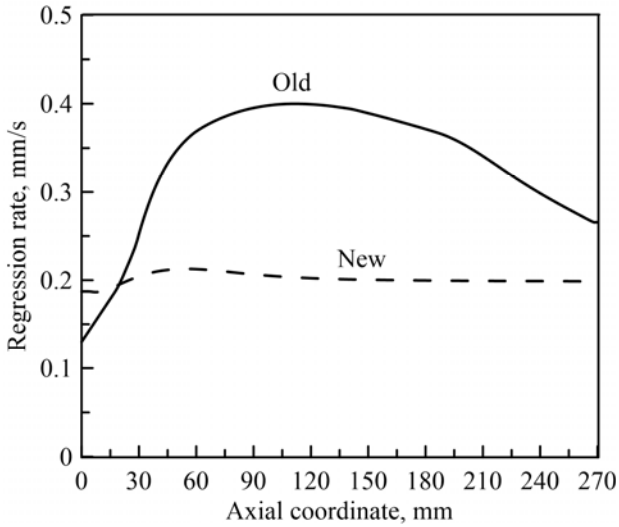

Figure 26 Comparison of the regression rate profiles obtained with the new and current prechamber configuration.

5. Conclusions

A CFD approach to the internal ballistics of hybrid rocket engines with integrated gas/surface interaction modelling for the prediction of the fuel regression rate has been presented. The RANS equations, with two additional transport equations for the average mixture fraction and its variance combined to the probability density function combustion model and thermochemical equilibrium are solved, coupled with a suitable sub-model to describe the fuel pyrolysis and regression, based on the local mass, energy and mixture fraction balance.

The main goal of the work was the development of a computational methodology able to capture the uneven regression rate and the value of the fuel consumption peak which were observed by injecting liquid nitrous oxide into single-port HDPE fuel grains in long firing tests (duration larger than 40s). Two test cases have been numerically reproduced with steady and quasi-steady transient simulations. In both cases, the numerical results show a fair agreement when compared to the experimental data. A discrepancy between the regression rate history and time-average regression rate was shown in one test, the explanation for which was recognized to be the influence of the ignition system. Furthermore, the model has been demonstrated to capture the fundamental features of the engine internal ballistics, which involve recirculation at the grain port inlet with the characteristic heat transfer mechanisms leading to a point of maximum regression rate, not only from a qualitative standpoint, as well as typical transient behavior, such as the trend of the local grain port diameter and of the local fuel regression rate during the engine operation.

The effect of the inlet temperature on the regression rate was also studied. Lower inlet temperatures affect the shape of the regression rate and the average value of the regression rate. Indeed, the jet spread angle of the incoming oxidizer, which defines the extension of the recirculation zone, increases with lower temperatures. The full decomposition temperature of nitrous oxide provides the best match of the numerical results with the experimental data, which consolidated the underlying assumptions.

Then, the results obtained with nitrous oxide were compared with those predicted when using oxygen and 85wt% hydrogen peroxide as oxidizers. While the average value and the shape of the regression rate is mostly similar for hydrogen peroxide and nitrous oxide, they differ significantly for gaseous oxygen. The analysis showed that the inlet velocity is a key parameter

for the regression rate, such that high velocities resulting from oxidizer decomposition, which suddenly lowers the gas density, increases the width of the recirculation zone, and consequently, the non-uniformity of the regression rate and the mixing.

Finally, a different prechamber configuration is considered in order to improve the engine design by reducing the non-uniformity of the fuel consumption.

6. Acknowledgement

This research was primarily funded by the Adaptable and Seamless Technology Transfer Program through Target-driven R&D (A-STEP) from Japan Science and Technology Agency (JST) Grant Number JPMTR20R6, and funded in part by the Research and Development Grant Program (Engineering) from the Institute of Space and Astronautical Science Japan Aerospace Exploration Agency (JAXA) and f3 Engineering Education and Research Center. This research was supported by the Ministry of Education, Science, Sports and Culture Grants-in-Aid for Young Scientists 20K14946, 2020 and Japan Society for the Promotion of Science (JSPS).

References

[1] L. Kamps, S. Hirai, H. Nagata, Hybrid Rockets as Post-Boost Stages and Kick Motors, Aerospace 8 (2021) 253.

[2] L. Kamps, K. Sakurai, Y. Saito, H. Nagata, Comprehensive Data Reduction for N2O/HDPE Hybrid Rocket Motor Performance Evaluation, Aerospace 6 (2019) 45.

[3] S. Ito, L. Kamps, H. Nagata, Fuel Regression Characteristics in Hybrid Rockets Using Nitrous Oxide/High-Density Polyethylene, J. Propuls. Power 37 (2021) 342-348.

[4] R. Okuda, K. Komizu, A. Tsuji, T. Miwa, M. Fukada, S. Yokobori, K.o Soeda, L. Kamps, H. Nagata, Fuel Regression Characteristics of Axial-Injection End-Burning Hybrid Rocket Using Nitrous Oxide, J. Propuls. Power 38 (2022) 759–770.

[5] G. Story, Large-Scale Hybrid Motor Testing. In Fundamentals of Hybrid Rocket Propulsion, 1st ed.; Progress in Astronautics and Aeronautics; Chiaverini, M., Kuo, K., Eds.; AIAA: Washington, DC, USA, 2006, Volume 218, 513–591.

[6] M. Kobald, U. Fischer, K. Tomilin, A. Petrarolo, C. Schmierer, Hybrid Experimental Rocket Stuttgart: A Low-Cost Technology Demonstrator, J. Spacecr. Rocket. 55 (2018) 484–500.

[7] D. Nakata, K. Yasuda, S. Horio, K. Higashino, A Fundamental Study on the Hybrid Rocket Clustering for the Rocket Sled Propulsion System, In Proceedings of the 52nd AIAA/SAE/ASEE Joint Propulsion Conference, Salt Lake City, Utah, 2016, 25–27 July.

[8] Y. Chen, B. Wu, Development of a Small Launch Vehicle with Hybrid Rocket Propulsion, In Proceedings of the 54th AIAA/SAE/ASEE Joint Propulsion Conference, Cincinnati, Ohio, 2018, 9–11 July.

[9] H. Gamal, A. Matusiewicz, R. Magiera, D. Hubert, L. Karolewski, K. Zielinski, Design, Analysis and Testing of a Hybrid Rocket Engine with a Multi-port Nozzle, In Proceedings of the 54th AIAA/SAE/ASEE Joint Propulsion Conference, Cincinnati, Ohio, 2018, 9‑11 July.

[10] G.A. Marxman, M. Gilbert, Turbulent boundary layer combustion in the hybrid rocket, Symp., Int., Combust. 9(1) (1963) 371–383.

[11] C. Carmicino, A. Russo Sorge, Role of Injection in Hybrid Rockets Regression Rate Behavior, J. Propuls. Power 21 (2005) 606-612.
[12] D. Bianchi, B. Betti, F. Nasuti, C. Carmicino, Simulation of Gaseous Oxygen/Hydroxyl-Terminated Polybutadiene Hybrid Rocket Flowfields and Comparison with Experiments, J. Propuls. Power 31 (2015) 919–929.
[13] D. Bianchi, F. Nasuti, C. Carmicino, Hybrid rockets with axial injector: Port diameter effect on fuel regression rate, J. Propuls. Power, 32, (2016) 984–996.
[14] V. Sankaran, Computational Fluid Dynamics Modeling of Hybrid Rocket Flowfields, Fundamentals of Hybrid Rocket Combustion and Propulsion, edited by K. Kuo, M. Chiaverini, Vol. 218, Progress in Astronautics and Aeronautics, AIAA, 2007, pp. 323–349.
[15] C. P. Kumar, A. Kumar, Effect of Diaphragms on Regression Rate in Hybrid Rocket Motors, J. Propuls. Power 29 (2013) 559–572.
[16] Y. S. Chen, T. H. Chou, B. R. Gu, J. S. Wu, Y. Y. Lian, L. Yang, Multiphysics Simulations of Rocket Engine Combustion, Comput. Fluids 45 (2011) 29–36.
[17] A. Coronetti, W. A. Sirignano, Numerical Analysis of Hybrid Rocket Combustion, J. Propuls. Power 29 (2013) 371–384.
[18] M. Lazzarin, F. Barato, A. Bettella, D. Pavarin, Computational Fluid Dynamics Simulation of Regression Rate in Hybrid Rockets, J. Propuls. Power 29 (2013) 1445–1452.
[19] B. Kim, Y. Na, K. Shin, C. Lee, Nonlinear Combustion and Fluid Mechanics in a Hybrid Rocket, J. Propuls. Power 28 (2012) 1351–1358.
[20] G. Lengellé, Solid-Fuel Pyrolysis Phenomena and Regression Rate, Part 1: Mechanisms, Fundamentals of Hybrid Rocket Combustion and Propulsion, edited by K. Kuo, M. Chiaverini, Vol. 218, Progress in Astronautics and Aeronautics, AIAA, 2007, pp. 127–163.
[21] M. Motoe, T. Shimada, Numerical Simulations of Combustive Flows in a Swirling-Oxidizer-Flow-Type Hybrid Rocket, 52nd Aerospace Sciences Meeting, National Harbor, Maryland, 2014, 13-17 January.
[22] D. Bianchi, F. Nasuti, Numerical Analysis of Nozzle Material Thermochemical Erosion in Hybrid Rocket Engines, J. Propuls. Power, 29 (2013) 547–558.
[23] G. Leccese, D. Bianchi, F. Nasuti, Simulations of Hybrid Rocket Flowfields Including Modeling of Fuel Pyrolysis and Thermal Radiation, 5th Space Propulsion Conference, Rome, Italy, 2016.
[24] G. D. Martino, C. Carmicino, R. Savino, Transient Computational Thermo-Fluid-Dynamic Simulation of Hybrid Rockets Internal Ballistics, J. Propuls. Power, 33 (2017) 1395-1409.
[25] G. D. Martino, C. Carmicino, S. Mungiguerra, R. Savino, The Application of Computational Thermo-Fluid-Dynamics to the Simulation of Hybrid Rocket Internal Ballistics with Classical or Liquefying Fuels: A Review, Aerospace 6 (2019) 56.
[26] G. Gallo, S. Mungiguerra, R. Savino, New Entrainment Model for Modelling the Regression Rate in Hybrid Rocket Engines, J. Propuls. Power 37 (2021) 893-909.
[27] G. Gallo, R. Savino, Regression Rate Model Assessed by Ballistic Reconstruction Technique in Hybrid Rocket Engines Burning Liquefying Fuels, Aerosp. Sci. Technol., 127 (2022) 107712.

[28] S. Hirai, L. Kamps, H. Nagata, Development of Safe, Low-Cost, Re-Ignitable Rocket Ignition System, AIAA Propulsion and Energy 2021 Forum, Virtual Event, 2021.

[29] C. Carmicino, G. Gallo, R. Savino, Self-Consistent Surface-Temperature Boundary Condition for Liquefying-Fuel-Based Hybrid Rockets Internal-Ballistics Simulation, Int. J. Heat Mass Transf. 169 (2020) 120928.

[30] A. J. Chorin, Numerical solution of Navier-Stokes equations, Math. Comput. 22 (1968) 745–762.

[31] T. Cebeci, Analysis of Turbulent Flows, second revised and expanded edition, Elsevier Ltd., The Boulevard, Langford Lane, Kidlington, Oxford, OX5 1GB, UK, 2004, pp.32–38.

[32] C. Truesdell, Rational Thermodynamic, McGraw-Hill, New York, 1984.

[33] F. R. Menter, Two-equation eddy-viscosity turbulence models for engineering applications, AIAA J. 32 (1994) 1598–1605.

[34] D. C. Wilcox, Turbulence energy equation models, in: Turbulence Modeling for CFD, DCW Industries, Inc. La Canada, California, 1998, pp.73–170.

[35] C. E. Wooldridge, G. A. Marxman, R. J. Kier, Investigation of Combustion Instability in Hybrid Rockets, NASA contract NAS 1-7310, Stanford Research Inst., 1969.

[36] Y. R. Sivathanu, G. M. Faeth, Generalized state relationships for scalar properties in non-premixed hydrocarbon/air flames, Combust. Flame 82 (1990) 211–230.

[37] W. P. Jones, J.H. Whitelaw, Calculation methods for reacting turbulent flows: a review, Combust. Flame 48 (1982) 1–26.

[38] R. W. Bilger, Turbulent Reacting Flows, Springer, Berlin, 1980, pp. 65-113.

[39] S. Gordon, B.J. McBride, Computer program of complex chemical equilibrium compositions and applications, NASA Ref. Publ. 1311 (1994).

[40] M. Chiaverini, Review of Solid Fuel Regression, Fundamentals of Hybrid Rocket Combustion and Propulsion, edited by Kuo, K., and Chiaverini, M., Progress in Astronautics and Aeronautics, Vol. 218, AIAA, 2007, pp. 49–93.

[41] D. Altman, R. Humble, Hybrid Rocket Propulsion Systems, Space Propulsion Analysis and Design, edited by R. W. Humble, G. N. Henry, and W. J. Larson, 1st ed., McGraw–Hill, New York, 1995, pp. 392–395.

[42] J. P. De Wilde, The Heat of Gasification of Polyethylene and Polymethylmethacrilate, Rept. PML 1988-C42, `SFCC Publ. 53, Faculty of Aerospace Engineering/Prins Maurits Lab./Solid Fuel Combustion Chamber, Delft Univ. of Technology, Delft, The Netherlands, Sept.1988.

[43] A. Karabeyoglu, B. J. Cantwell, J. Stevens, Evaluation of Homologous Series of Normal-Alkanes as Hybrid Rocket Fuels, AIAA Paper 2005-3908, July 2005.

[44] P. J. Roache, Verification and Validation in Computational Science and Engineering, Hermosa Publishers, Albuquerque, New Mexico, 1998.

[45] C. Carmicino, A. Russo Sorge, Influence of a Conical Axial Injector on Hybrid Rocket Performance, J. Propuls. Power, 22(5) (2006) 984-995, https://doi.org/10.2514/1.19528.

[46] C. Carmicino, F. Scaramuzzino, A. Russo Sorge, Trade-off between paraffin-based and aluminium-loaded HTPB fuels to improve performance of hybrid rocket fed with N2O, Aerospace Science and Technology, 37(2014), 81–92, https://doi.org/10.1016/j.ast.2014.05.010